Experimental study of a preshower module and its readout system - Testbeam and testbench results

Ziad Zj Ajaltouni, G. Bohner, R. Bonnefoy, C. Carloganu, R. Cornat, O. Deschamps, M. Fiandino, R. Langon, J. Lecoq, R. Lefevre, et al.

LHCb 2003-018 CALO
February 2003

Experimental Study of a Preshower Module and its Readout System

— Testbeam and Testbench Results —

Z. Ajaltouni, G. Bohner, R. Bonnefoy, C. Cârloganu, R. Cornat, O. Deschamps, M. Fiandino, R. Langon, J. Lecoq, R. Lefèvre, S. Monteil, P. Perret, C. Rimbault

Laboratoire de Physique Corpusculaire - Clermont-Ferrand

ABSTRACT

The performances of the LHCb preshower detector have been extensively studied with cosmic rays and beam data. Both the light system (scintillator tiles, fibres and MAPMT) and the electronic readout (Very Front End and Front End) have been investigated. During the 2002 testbeam campaigns, the complete readout electronic chain has been tested in realistic conditions for the first time. This note aims at summarising the experimental status of the preshower system drawn so far.

1 Introduction

The LHCb calorimeter system comprises four consecutive semi-projective detectors: the scintillator pads (SPD), the preshower (PS), the electromagnetic (ECAL) and hadronic (HCAL) calorimeters (see figure 1).

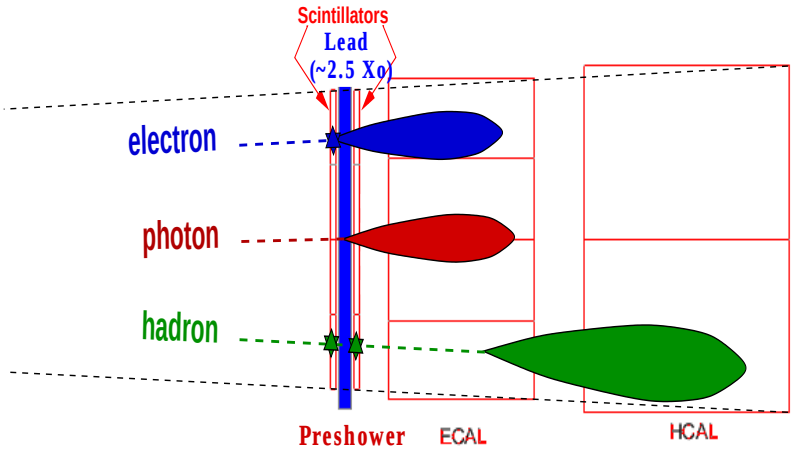

Figure 1: Longitudinal view of LHCb calorimeter system.

The SPD and PS detectors are two scintillator planes placed before and, respectively, after a lead sheet of 2.5 radiation lengths. Each has 6000 channels, designed for a one-to-one correspondence with the ECAL towers, in a projective geometry (see figure 2).

The main task of the SPD and PS detectors is to validate the electromagnetic nature of the ECAL showers, especially for the Level 0 trigger. The hadronic shower rejection is based on a low threshold applied on the PS signal, while the single bit SPD information allows the tagging of the charged or neutral origin of the electromagnetic showers. The PS energy measurement will be also used for offline improvements of the ECAL measurement.

The scintillation light from a SPD and, similarly, a PS cell, is extracted with a wavelength shifting (WLS) fibre that turns in a groove machined into the scintillator pad. Both fibre ends are connected to a pixel of a 64 anode photomultiplier tube (MAPMT), located above or below the detector, through long clear fibres.

The readout system for PS consists of the Very Front End (PSVFEE) and the Front End (PSFEE) electronic boards. The first board shapes the analog signals, whereas the second digitises them and treats the digital signals.

Large dynamics and high accuracy are required for the readout electronics in order to allow measurements of large electromagnetic energies (up to the equivalent of the energy deposited by 100 minimum ionizing particles, hereafter called "MIPs"), while being able to apply a low trigger threshold in the five MIPs range. Lower signals of one MIP (about 20 photoelectrons) should also be used for energy calibration.

A 10 bits digitisation, together with a MIP/10 least significant bit (LSB) precision has been shown to fulfill these dynamics requirements [1]. The main challenge of the preshower readout electronics is then to handle small signals with erratic shapes, due to a small number of photoelectrons. For this, the analog Very Front End board [2] includes specially designed ASICs with 40 MHz integrators, able to shape fluctuating pulses. In addition, the system is required to allow successive triggers, even if the duration of the

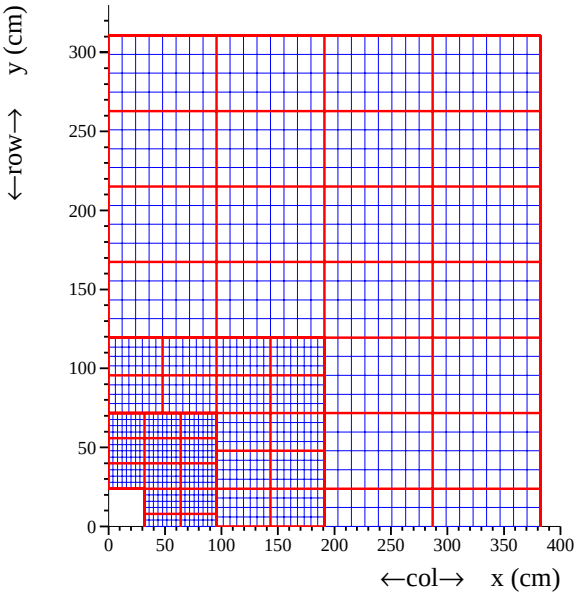

Figure 2: Transversal segmentation of a Ps quarter. Each square is a Ps cell of 4×4 cm^2 in the inner region, 6×6 cm^2 in the middle and 12×12 cm^2 in the outer one.

Ps pulses is larger than 25 ns, which is the time difference between consecutive bunch crossings at LHC [3]. For this, the digital Front End board [4] subtracts the estimated remnant from the previous 25 ns cycle (α correction).

Both the upstream (light system: preshower tiles, fibres, and MAPMT) and downstream (Very Front End and Front End electronics) readout systems have been extensively studied. This note aims at summarising the experimental status of the preshower system, as it was drawn so far from testbeam campaigns and test bench studies.

Of major importance for the readout design is the temporal shape of the Ps pulses. Section 2 overviews therefore the theoretical pulse shape and its implications on the readout system. The experimental test setups are described in section 3. The following sections report on the experimental results of the Ps studies. In the order of appearance, the treated items are: pedestals, pulse shape, Ps cell uniformity, light yield, MAPMT gain, integrator gain uniformities, crosstalk.

2 Pulse shape and readout functionalities

Theoretically, the average time structure of the light pulse at the MAPMT entrance could be drawn from the following considerations:

- The fluorescence decay times in the fibres and in the scintillator tiles are respectively $\tau_{\text{fibre}} \sim 10$ ns and $\tau_{\text{tile}} \sim 2$ ns. The convolution of the scintillation time in the scintillator tile with the photon propagation in the fibre leads to a pulse shape characterised by a fast rising time $t_{\text{max}} = \frac{\ln(\tau_{\text{fibre}}) - \ln(\tau_{\text{tile}})}{1/\tau_{\text{tile}} - 1/\tau_{\text{fibre}}} \sim 4$ ns, followed by a $\tau_{\text{fibre}} \sim 10$ ns exponential decay.

- the homogeneously distributed fluorescence sites along the fibre length coiled inside the tile leads to a time spread given by L/v where L is the fibre length holden in the scintillator groove and v the light celerity inside the fibre. Depending of the Ps cell size, which varies from 4×4 cm^2 to 12×12 cm^2, the L/v spread accounts for 2 to 4 ns.

Within this description, the average light shape can be seen as a sum of exponential functions displaced in time:

$$S(t) \propto \int_0^{L/v} \Theta(t - t_0)(e^{-\frac{t-t_0}{\tau_{fibre}}} - e^{\frac{t-t_0}{\tau_{tile}}})dt_0$$

$$\text{where} \quad \Theta(t - t_0) = \begin{cases} 0 & \text{when} \quad t - t_0 < 0 \\ 1 & \text{when} \quad t - t_0 > 0 \end{cases}$$

is the Heaviside function. A graphical representation of such a pulse can be seen in figure 3.

On average about 90 % of such a pulse is contained in the 25 ns of a bunch crossing cycle.

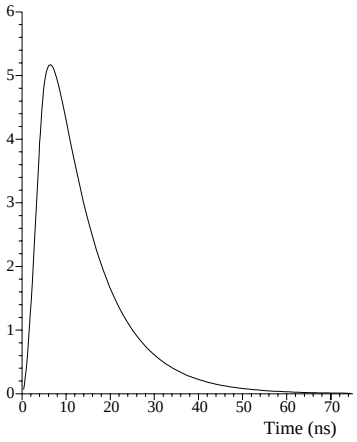

Figure 3: Theoretical light shape.

However, such a basic analytical approach is obviously a poor approximation: several additional factors in production, attenuation, propagation and conversion of photons have to be added. The MAPMT time response should also be included. In practice, a refined simulation [5] based on Monte-Carlo methods has been used to produce a more realistic shape. For this more realistic pulse shape, the integrated signal fraction over 25 ns decreases on average to about 80 %.

The dispersion of this fraction is however large and it scales as the inverse square-root of the number of photoelectrons: it reaches the 10 % level for MIP signals due to the small amount of photoelectrons produced and it is at 4 % level at trigger threshold for electromagnetic showers (5 MIPs). For larger signals the residual pulse is even better defined but the non negligible pulse residue above 25 ns can fulfill the Level 0 trigger criteria during several cycles of consecutive bunch crossings. As example, a 100 MIPs signal leads to a $\sim$ 15 MIPs residue into the following bunch crossing cycle. This residual pulse could, in addition, spill over a possible consecutive signal.

The pulse residue has thus to be subtracted by the readout system. The subtraction is naturally performed by the PSFEE board, which subtracts also the pedestals and corrects the gains [4]. This subtraction is done according to the following considerations.

Let $S^j(t)$ be the signal of bunch crossing j. Integrating this pulse during 25 ns, $s^j_{25} = \int_{t_j}^{t_j+25} S^j(t)dt$, leads to a fraction β^j_0 of the global integral, $s^j_\infty = \int_{t_j}^{\infty} S^j(t)dt$. Taking into account overlapping residues from preceding bunch crossings, the effective 25 ns integral for the bunch crossing j becomes:

$$s^j_{eff} = \beta^j_0 s^j_\infty + \beta^{j-1}_1 s^{j-1}_\infty + \beta^{j-2}_2 s^{j-2}_\infty + ... = \beta^j_0 s^j_\infty + \sum_{i>0} \beta^{j-i}_i s^{j-i}_\infty \qquad (1)$$

where β^{j-i}_i is the residual fraction of the signal from the bunch crossing $j - i$, s^{j-i}_∞, into the bunch crossing j, as shown on figure 4.

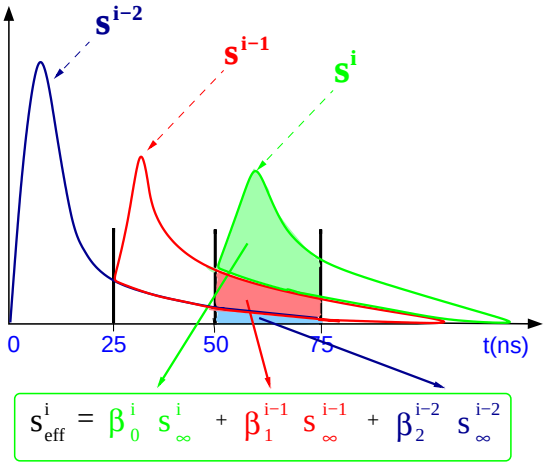

Figure 4: Overlap of signals from consecutive bunch crossings.

Let α be the ratio of the fractions of the signal from a given bunch crossing integrated in two successive samples:

$$\alpha = \int_{t_0+25}^{t_0+50ns} S(t)dt / \int_{t_0}^{t_0+25ns} S(t)dt$$

If the raising time is neglected, the pulses are almost exponential and α is constant in time and pulse independent. It is the same for β_i^{j-i}'s, which can be therefore simply written as β_i. One has $\beta_i \sim (1-\alpha)\alpha^i$ and in particular $\beta_0 \sim (1-\alpha)$. Equation (1) becomes then:

$$\begin{aligned}
(1-\alpha)s_\infty^j &= s_{eff}^j - (1-\alpha)\sum_{i>0}\alpha^i s_\infty^{j-i} \\
&= s_{eff}^j - (1-\alpha)\alpha s_\infty^{j-1} - (1-\alpha)\sum_{i>1}\alpha^i s_\infty^{j-i} \\
&= s_{eff}^j - (1-\alpha)\alpha s_\infty^{j-1} - (1-\alpha)\sum_{i>0}\alpha^{i+1} s_\infty^{j-(i+1)} \\
&= s_{eff}^j - \alpha[(1-\alpha)s_\infty^{j-1} + (1-\alpha)\sum_{i>0}\alpha^i s_\infty^{j-1-i}]
\end{aligned}$$

Recursively one also has:

$$(1-\alpha)s_\infty^{j-1} = s_{eff}^{j-1} - (1-\alpha)\sum_{i>0}\alpha^i s_\infty^{j-1-i}$$

and by subtracting the last two equations,

$$\boxed{s_\infty^j = (1-\alpha)^{-1}(s_{eff}^j - \alpha s_{eff}^{j-1})}$$

where $(1-\alpha)^{-1}$ is a global factor that can be absorbed in the signal calibration. The subtraction of the preceding bunch crossing residues from the current bunch crossing signal can then be performed easily by the Front End readout system.

Obviously, the above treatment is oversimplified. Mainly due to raising time effects, β_0, also called β in the following, is slightly different from $1-\alpha$ for realistic pulses. But

as long as the preshower signal follows the assumed quasi exponential shape behavior, the single parameter correction is correct.

One of the main goals of the measurements summarised in the present note was to check the validity of the approximated treatment described above.

3 Experimental setups

3.1 Cosmic rays test bench

A Ps prototype module made of 16 large size tiles has been studied in the lab, using the energy deposited by cosmic rays. A dedicated test bench, sketched on figure 5, has been developed for this purpose. It consists in a module, similar to the module prototype studied in testbeam, made of 16 tiles of 12×12 cm^2, from which the scintillation light is extracted through 80 cm long WLS fibres coupled to 3 m long clear fibres.

The light yield of the 16 channels is read out sequentially with a single monoanode R-5900 PMT [6]. A specially designed mask connector allows the selection of the channel to be read while the others are blocked off.

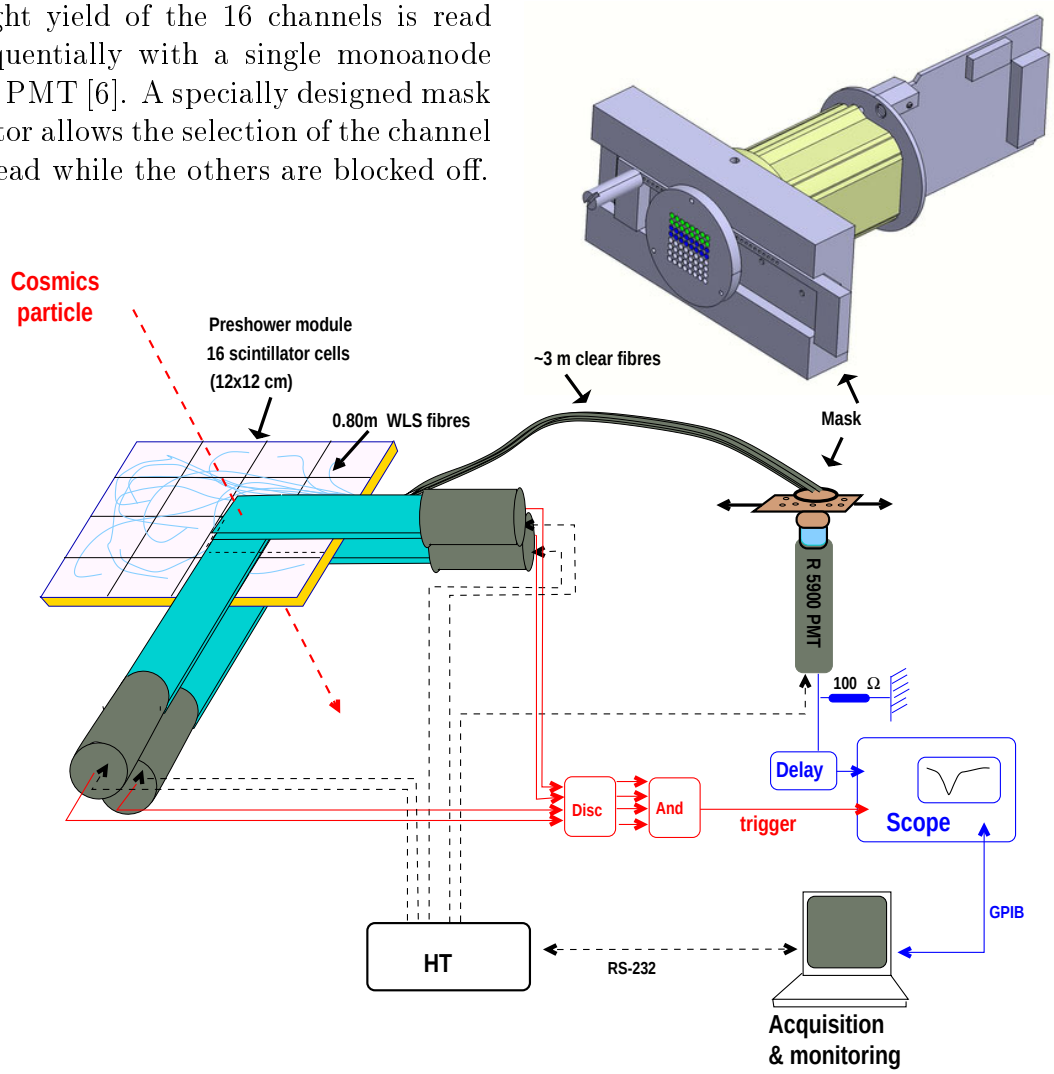

Figure 5: Cosmic rays test bench setup. The specially designed PMT connector allowing us to choose the fibre to be read is shown on the top right of the figure.

Two of the 16 cells of the module are instrumented with LEDs, making possible a dedicated study of the cell to cell crosstalk inside the module. In addition, the clear fibres can be removed and the light can be read directly on the WLS fibre connector thanks to a specially designed PMT mask connector similar to the one sketched on the top right of figure 5.

The PMT pulse is read out with a scope through a 100 Ω load resistor. The acquisition is triggered by a coincident signal from a system of scintillators covering a $\sim 10 \times 10$ cm^2 area on the module surface. A PC acquires the pulse recorded by the scope and monitors the PMT high voltage supply.

The signals recorded by the scope consist of 500 (time,voltage) points with a time resolution of 0.4 ns, allowing a fine study of the pulse shape over 200 ns. Typical PMT outputs, which are very erratic, are shown on figure 6, left, whereas on the right of the same figure can be seen the mean pulse shape, as it was obtained by averaging 1300 cosmic signals.

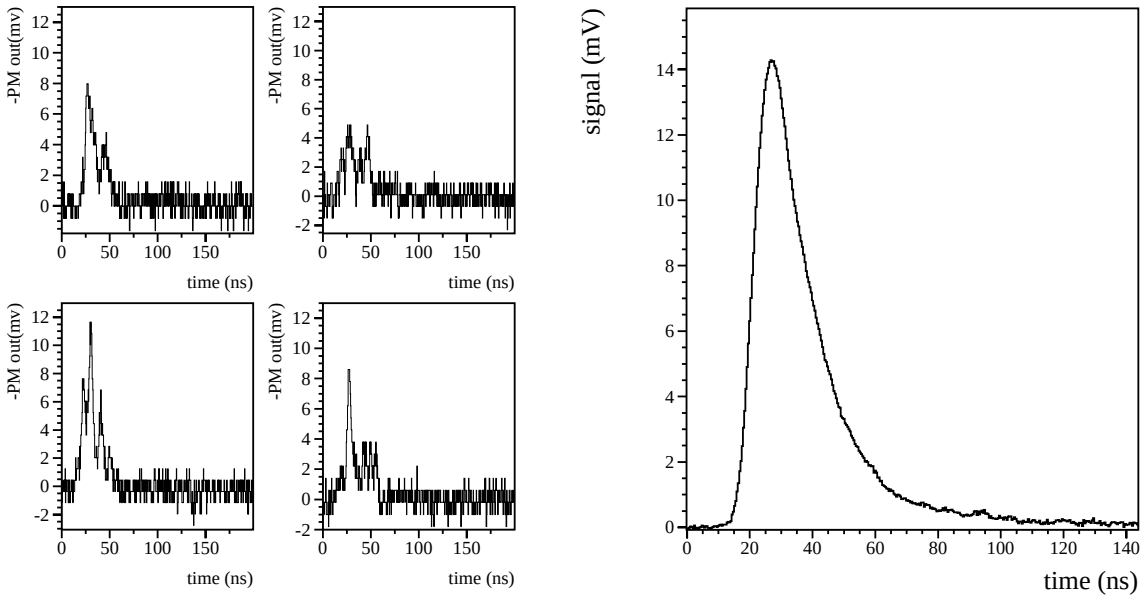

Figure 6: *Left:* individual signals from cosmic particles as an illustration of the large fluctuations due to the low number of photoelectrons per MIP. *Right:* mean pulse shape averaged over 1300 cosmic signals.

The pulse rising front is shifted with respect to the beginning of the scope recording in order to use the first nanoseconds for offline computation of the mean pedestal value. As it can be seen on figure 7, the pedestal noise is at the level of 0.2 mV.

In order to extract the relevant parameters for the preshower readout system, a 25 ns sampling is performed offline on the scope pulses. The starting time of the sampling, t_0, is obtained as shown on figure 8: the curve integrating the PMT output as function of time is first computed, then the tangent line of this primitive at 5 % of its maximum is considered. Finally, t_0 is defined as the time value where this tangent line crosses the abscissa. The dispersion of t_0 defined in this way is about 2 ns, as it can be seen on figure 8.

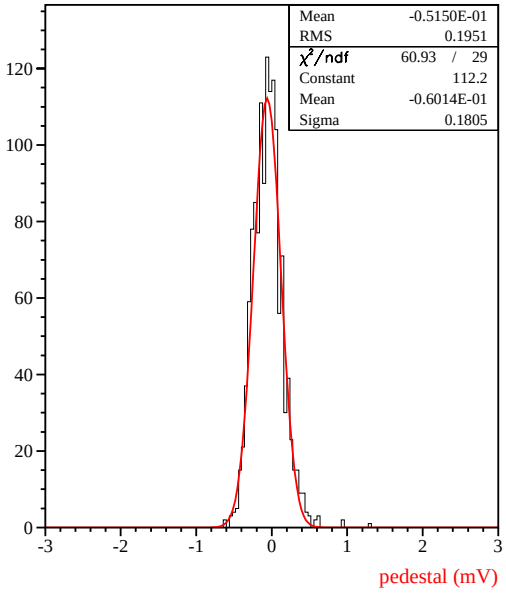

Figure 7: Pedestal distribution.

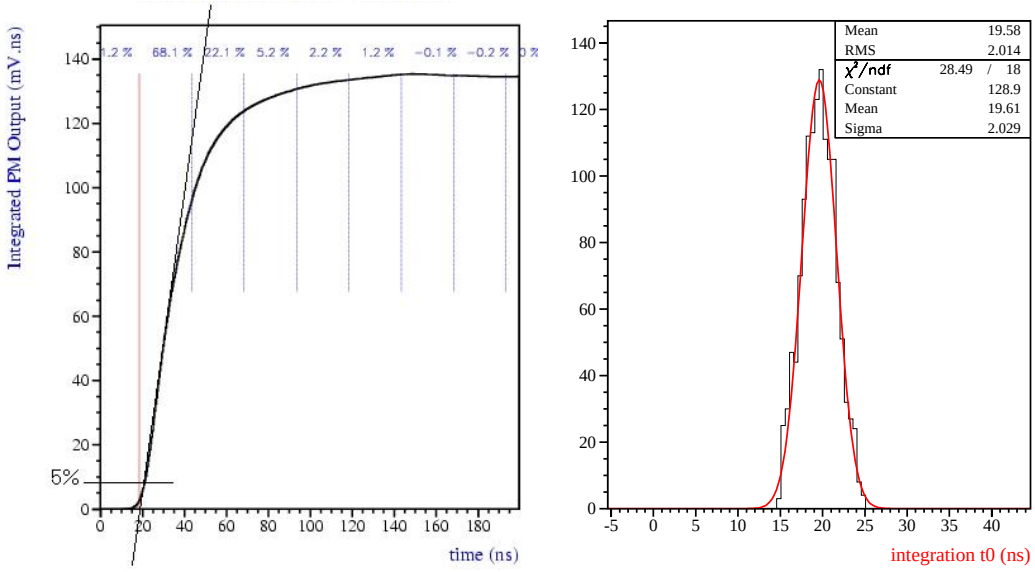

Figure 8: *Left:* determination of the pulse initial time t_0 from the pulse primitive. Also shown is the 25 ns sampling according to t_0. *Right:* t_0 distribution.

3.2 Testbeam

Several testbeam periods in the X7 area at CERN have been allocated for testing Ps modules and Ps readout electronics. In 2002, the full readout chain, including prototypes of both PSVFEE and PSFEE boards, has been used for the first time in realistic conditions. Testbeam results presented in this note concern the two corresponding testbeam periods, June and August 2002.

A global sketch of the testbeam setup is drawn on figure 9. The Ps module prototype included 16 scintillator tiles of 12×12 cm^2. The scintillation light was extracted through 80 cm long WLS fibres, read both ends by a MAPMT through 3 m long clear fibres. The MAPMT mask, which ensures the optical connection between the clear fibres and the MAPMT, with its 4×4 instrumented pixels, is shown on the top right of figure 9.

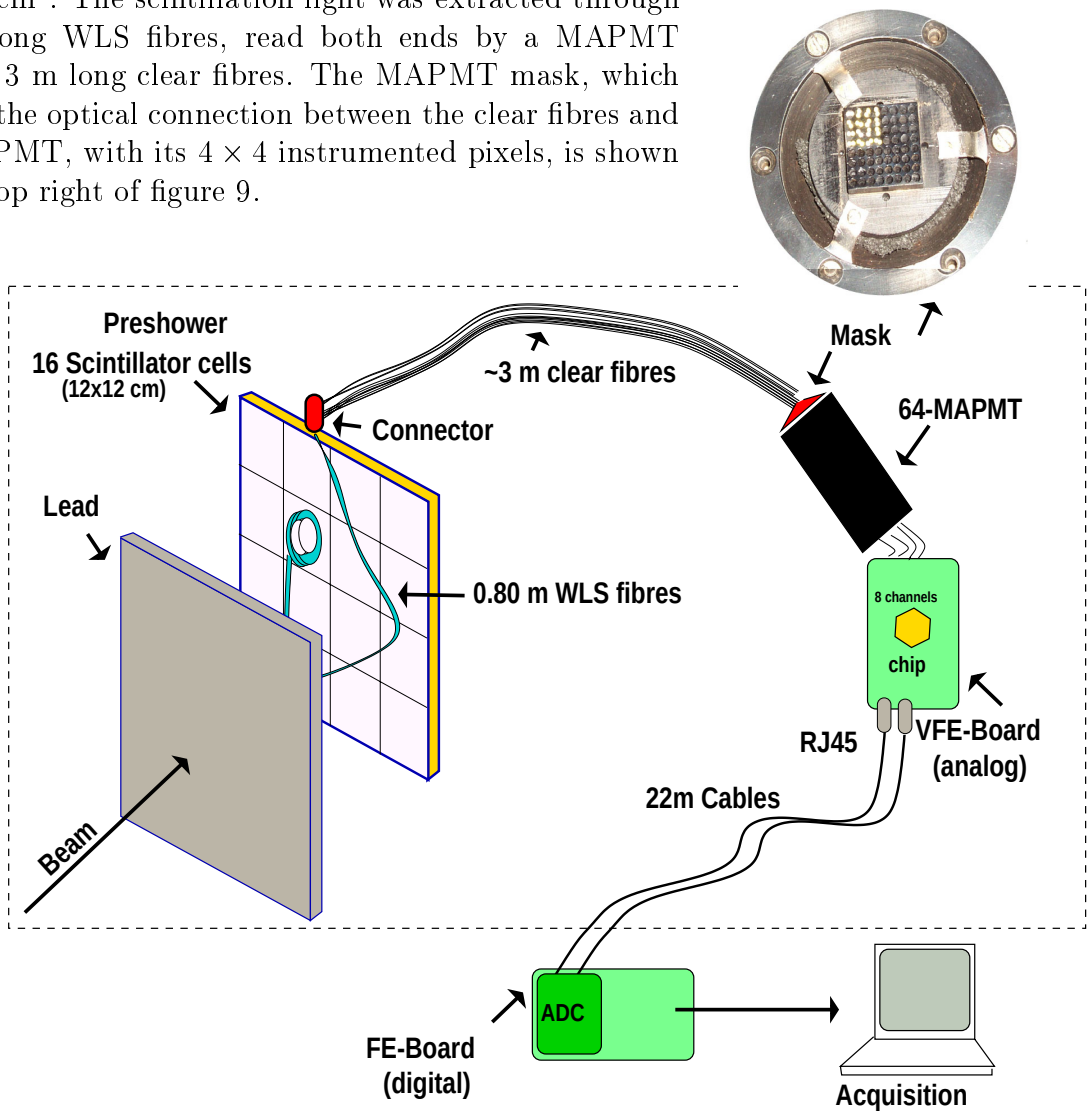

Figure 9: Test beam global setup. The MAPMT mask is shown on the top right of the picture. Its instrumented quarter of 4×4 pixels out of a total of 64 can be seen.

The MAPMT mask was aligned with the MAPMT window through optical crosstalk measurements. A good alignment was considered to lead to similar crosstalk signals in adjacent and symmetrical MAPMT channels. However, this alignment procedure is not

optimal, since a possible slight rotation of the mask and gain non uniformities between channels were not taken into account during the alignment procedure.

The PSVFEE board performed the pulse integration over 25 ns and 22 m long Ethernet cables carried its 16 differential analog outputs to the PSFEE board situated in the barracks. Special features have been added to the PSFEE prototype, allowing the acquisition and the monitoring of the board through a PC. For the testbeam purposes a bare bones signal processing has been used: the pedestal and the α correction were not applied. No corrections for the gain dispersion within the 16 channels were performed neither and the 10 bits to 8 bits transcoding was shortcut. The PSFEE prototype was steered by a Linux PC using the VME bus and the bus itself communicates with the PC through the PCI-MXI2 board from National Instruments.

A complete data acquisition program was developed in *C++* [7]. It makes use of the threads to perform continuous data acquisitions, while allowing user run control and real time monitoring of the data. The graphical user interface is based on the ROOT [8] GUI classes, which has the benefit of allowing straightforward adds of analysis modules based also on ROOT.

Data were taken with MIP beams (muons or charged pions) as well as with electrons, with or without a 1 cm lead sheet in front of the scintillator module. The acquisition trigger used the usual testbeam facility based on the coincidence of signals from two PMTs situated in front of the module under study.

Because the available beam was not clocked, an external 40 MHz clock was distributed to the PSVFEE and PSFEE boards. A 3.5 nanoseconds window was opened for a beam particle to trigger the acquisition. The integration starting time with respect to the signal pulse was tuned by changing the delay between the trigger window and the clock signal. However, the trigger window width resulted in an equivalent 3.5 ns jitter in the start of signal integration within the PSVFEE board. The window width slightly affects the time related measurements of the pulse presented here, but does not change the main conclusions that can be drawn.

The ADC sampling time was also tuned using a delay module and set in the middle course of the PSVFE 25 ns quasi-squared signal, to avoid a sampling shift caused by a possible ADC jitter.

For testbeam purposes, each cell of the preshower module has been instrumented with a blue LED and LED data were taken to calibrate the light yield. This required a slightly modified trigger setup using a pulse generator firing the LEDs and providing a trigger signal for the acquisition. By unplugging the LEDs, it was also used as a random trigger signal for pedestal runs.

Throughout this note, an acquisition *run* has to be understood as the recording of a set of *events* (usually 500-2000 events/run) within identical conditions. An *event* is meant as N consecutive *samples* (a *sample* corresponds to the digitised value of the charge integrated over 25 ns), with N defined at the run level. In practice, events were defined on the basis of 16 or 32 samples, leading to sampling sequences over 400 or 800 ns. The signal position within the N samples is set online around the middle course of the sequence, in order to keep the few first samples for offline computation of the mean pedestals. Figure 10 displays typical outputs of the testbeam acquisition and offline treatment.

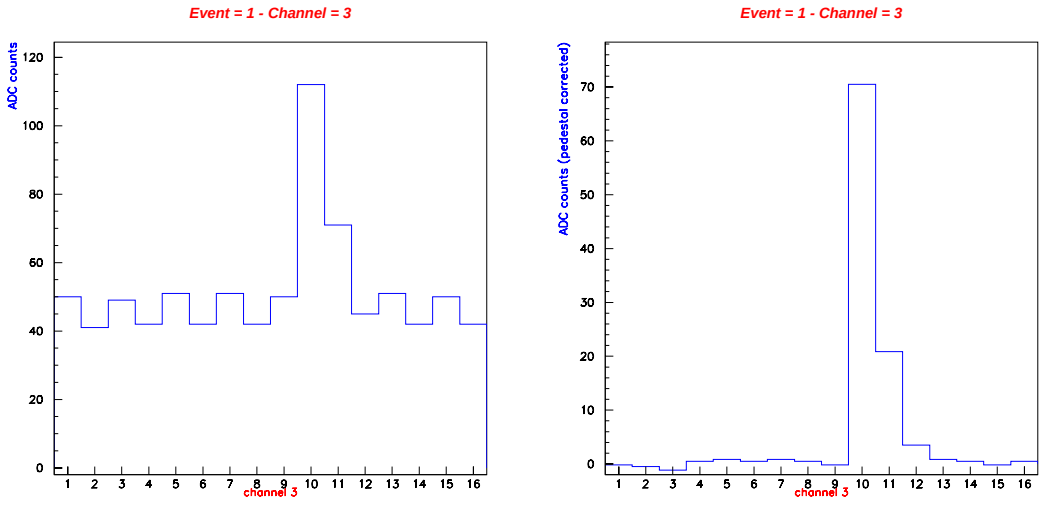

Figure 10: *Left:* a raw testbeam event (sequence of 16 consecutive 25 ns samples). *Right:* same event after offline subtraction of the pedestals.

4 Pedestal stability

The pedestals were extensively checked both during dedicated runs and along with the data taking runs. Indeed, since for each event 16 samples were recorded and the signal was centered in the event window, the first samples have only pedestal contributions. It is not the case for the last samples, which see the tail of the signal.

In the PSVFEE board prototype, two chips, each handling eight channels, perform the signal shaping of the 16 instrumented MAPMT outputs. The shaping method uses two interleaved fast integrators, each working at 20 MHz: while one integrates the MAPMT signal during 25 ns, the second is digitally reset. This leads to two different offsets per channel, depending on which integrator was used or, said it differently, to different pedestal offsets for odd and even samplings in the event sequence. Generally, the two integrators of one channel have noticeably different pedestals and this difference was used in order to decide, for each event, about the integrator corresponding to each sample: averaged pedestal values were calculated for odd, respectively even samples; if the average for the odd samples was lower, they were assigned to the lower pedestal integrator, etc.

A dedicated pedestal run of 500 events takes about 2 s, to be compared with ~ 5 min for a pion run with the same statistics. No drifts of the pedestal values are observed during the runs (figure 11, left). The distributions are fitted by gaussians with spreads around 0.7 ADC counts (figure 11, right) and the mean values are used for the pedestal subtraction.

A pedestal run of eight hours was performed in the middle of the test beam period. As it can be seen on figure 12, for one of the channels, the pedestals are constant within 0.5 ADC counts. No drifts are noticeable in the noise distribution either.

Using also the data runs, it was possible to check the longer term stability. As it can be seen on figure 13 which monitors variations over three days of data taking, fluctuations exist, but they are within the electronic noise and well below the least significant bit.

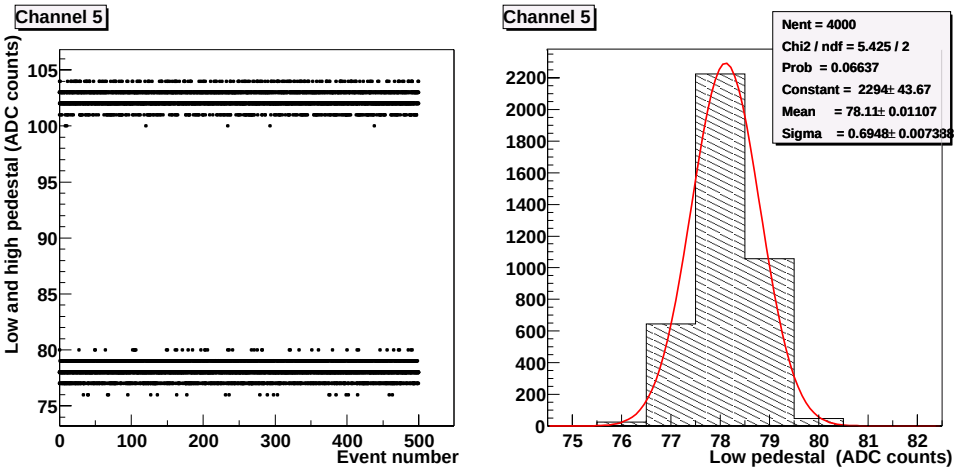

Figure 11: *Left:* variation of the pedestals as function of time (proportional with the event number). No drift is noticeable. *Right:* the measured pedestal values are gaussian, with a spread of ~ 0.7 ADC counts. An ADC count accounts for 1 mV.

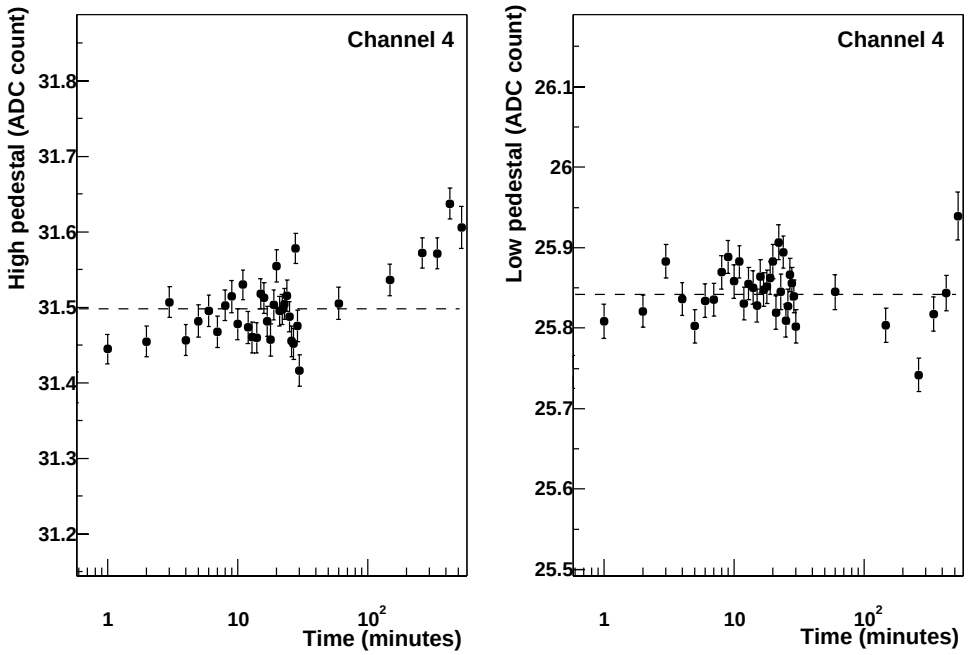

Figure 12: Mean pedestal values (in ADC counts) vs. time (in minutes).

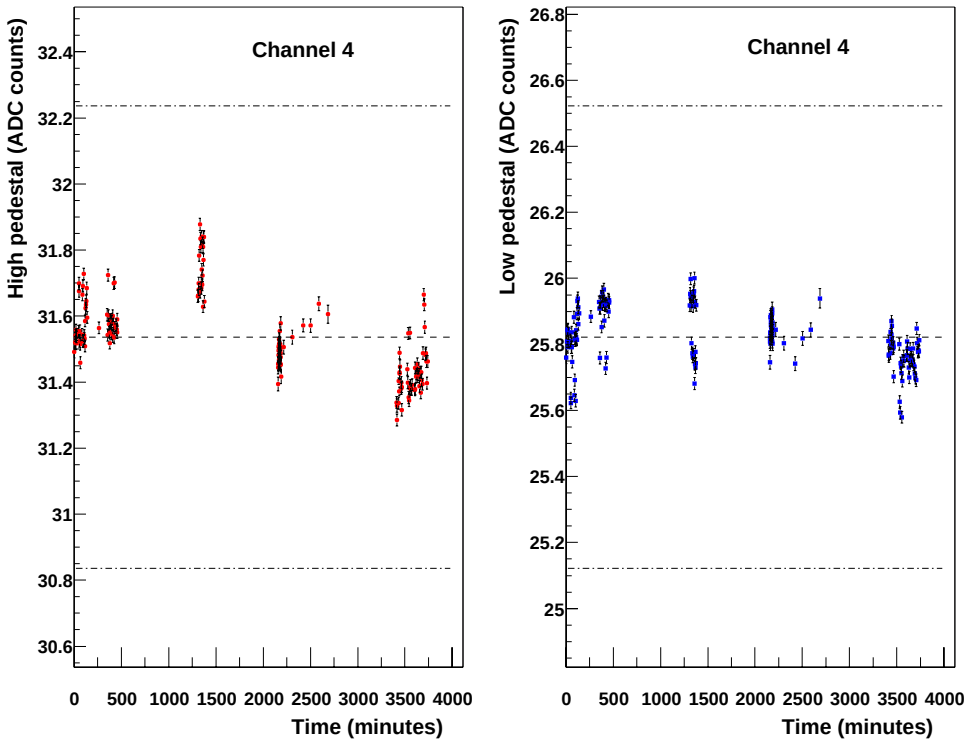

Figure 13: Mean pedestal values (in ADC counts) vs. time (in minutes) for channel 4.

5 Pulse shape time characteristics

Of major importance for the LHCb experiment, due to the fast 40 MHz readout, the pulse shape of the Ps has been extensively studied. The response of the Ps cells to MIPs was measured both in testbeam and in the cosmic rays test bench. The testbeam electron data allowed also checks of signal distortions with the pulse height. The long term behavior of the signal was also scrutinised.

5.1 Signal shape for MIP signals

Since the signal is integrated only over a fraction (25 ns) of its duration and its raising time is very fast, the charge collected depends critically on the integration starting time, t_0 and so do α and β (defined in Section 2). The procedure is to set t_0 such that the charge collected within 25 ns is maximal and to measure α and β for this definition of t_0.

5.1.1 Scan of the integration starting time

During August 2002 testbeam period, a scan of the integration starting time, t_0, has been performed on the different cells of the Ps module prototype, in order to check possible dispersions in the arrival time of the signals.

The integration window was changed using an adjustable delay between the trigger signal and the 40 MHz clock used both by PSVFEE and PSFEE boards. This delay was varied from 0 ns to 24 ns by steps of 2 ns. MIP signals were obtained from 100 GeV pions by removing the lead sheet from the Ps. The MAPMT high voltage was fixed to

800 V for the measurements presented in the following, but similar results were found for other values.

Figure 14 shows the fraction of signal integrated in five successive samples as function of t_0, for 13 different cells. The result of the refined simulation mentioned in section 2 is superposed to the data. The curves are replicated every 25 ns. The total charge, S_{tot} was estimated by summing the charge collected over all the 16 samples of the event and β_i is defined as the ratio between the signal in sample i, S_i, and S_{tot}. The samples are numbered with respect to the one which integrates the most of the signal and which is referenced as sample 0. Sample -1 and sample 1 are, for example, the samples just before and respectively just after the main one.

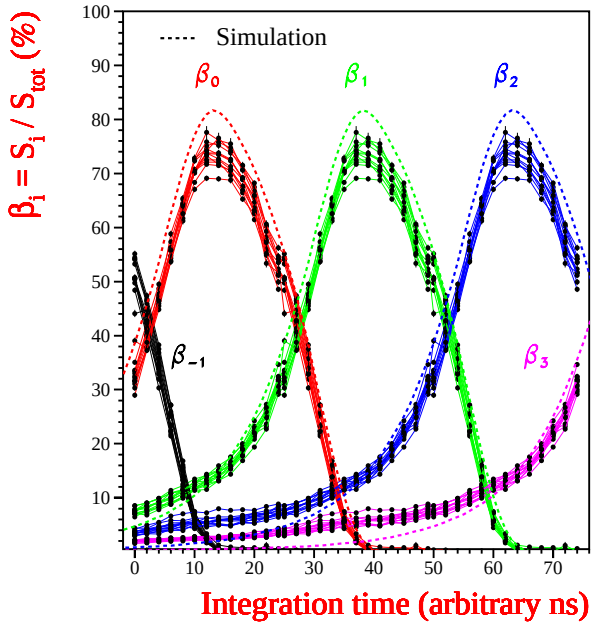

Figure 14: Fractions of signal integrated in five successive samples as a function of the integration starting time. The measurements are superposed for 13 different channels. The dotted lines are the result of the refined simulation from [5].

The estimation of S_{tot} from the charge collected over the 16 samples of the event is equivalent to integrating the first 175 ns of the signal. As it will be shown in subsection 5.2, the signals are in reality longer, but the integrated charge after the first 175 ns is negligible.

Figure 14 shows that t_0 for which β_0 reaches its maximum is the same within $\pm$ 1 ns for all cells. The integration starting time was therefore set to the same value for all channels. The curves exhibit slight discontinuities at replication time due to the integrator dead time, which is of the order of 1 ns and leads therefore to an effective integration time around 24 ns.

It is worthwhile to note that with this choice of t_0, about 14 % of the signal is recorded in the next to the main sample and that the precursor β_{-1} that can be seen in the previous sample was measured to be of the order of 0.5 %, which is sufficiently small.

Maximal β_0 is found to be around 73 % on average and to vary from 69 to 75 % according to the channel, which is quite low compared to the 82 % given by the simulation. Several factors could explain the difference between data and the Monte Carlo simulation:

- the integrator dead time. Since the charge collected in one sample increases with the integration time, the upper limit for the integrator dead time contribution can be estimated by multiplying the charge collected in sample 0 by 25/24, while keeping the others unchanged. $\beta_0 = 73$ % becomes then 73.8 %, i.e. a 0.8 % shift.

- the time jitter of testbeam data with respect to the 40 MHz clock, which was measured to be of 3.5 ns (min to max). By taking into account this jitter in the simulation (using a flat distribution), the decrease obtained in the value of β_0 was up to 0.8 %.

- a non negligible RC of the readout. The capacity of the readout is dominated by the PSVFEE board contribution and is of the order of 10 pF. As 150 Ω load resistors were used, the RC of the readout is around 1.5 ns. This affects the pulse raising time and leads to a decrease of β_0 of 1.7 % with respect to β_0 for an ideal readout with negligible RC.

These three contributions can therefore account only for 3.5 % of the 9 % difference between data and simulation. The remaining effect is likely due to a long term contribution to the signal, observed in the data, but absent from the simulations. This is consistent with the fact that for t_0 which maximises β_0, the measured β_2 and β_3 are around 5 % and 2 % respectively, while the simulation predicts 2 % for β_2 and a negligible β_3. By summing the differences between data and simulation from β_2 up to β_6 (the last recorded sample), a global difference of 7 to 8 % is obtained, which explains the 5.5 % remaining in the difference between data and simulation ($[73 + 3.5] \times 1.075 \approx 82$). This long term component is studied in more details in subsection 5.2.

5.1.2 α, β for MIP signals

The integration starting time being chosen, the most important parameters of the pulse shape are the fraction of signal recorded in the main sample, $\beta = S_0/S_{tot} = \beta_0$, and the ratio between the next to the main sample and the main one, $\alpha = S_1/S_0 = \beta_1/\beta_0$. In LHCb, in order to maintain a reasonable photostatistics, while recording only the main sample, and in order to limit the spill-over effects, large β and small α are mandatory. Not only central values of β and α are important, but also their fluctuations from one event to another, since they affect respectively the Ps energy resolution and the accuracy of the spill-over correction performed in the PSFEE board.

β and α central values and event by event fluctuations were estimated for MIP signals. As it can be seen in figures 15 and 16, left, where Gaussian fits are superposed to the data, the distributions are not Gaussian. β, α central values and RMS were therefore estimated directly from the measured distributions and not from the Gaussian fit.

The same figures show also the distribution of β and α mean values and RMS for the 15 cells studied. The mean values are respectively 72.9 % for β and 21.0 % for α. For the implementation of the spill-over correction in the PSFEE board, it should be noted that none of the cells has a mean α greater than 24 %.

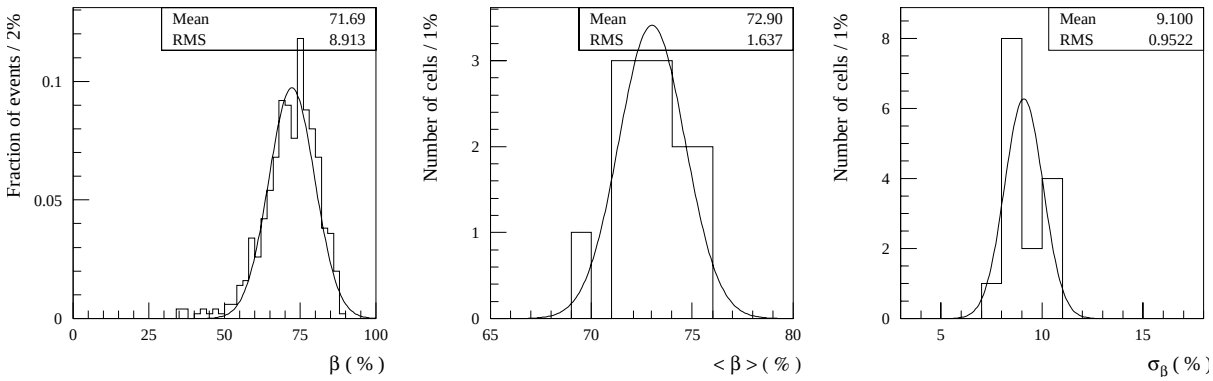

Figure 15: *Left:* typical distribution of β for MIPs. *Centre:* distribution of β mean value for MIPS over the 15 Ps cells studied. *Right:* distribution of β RMS for the same 15 Ps cells. Gaussian fits are superposed on the distributions.

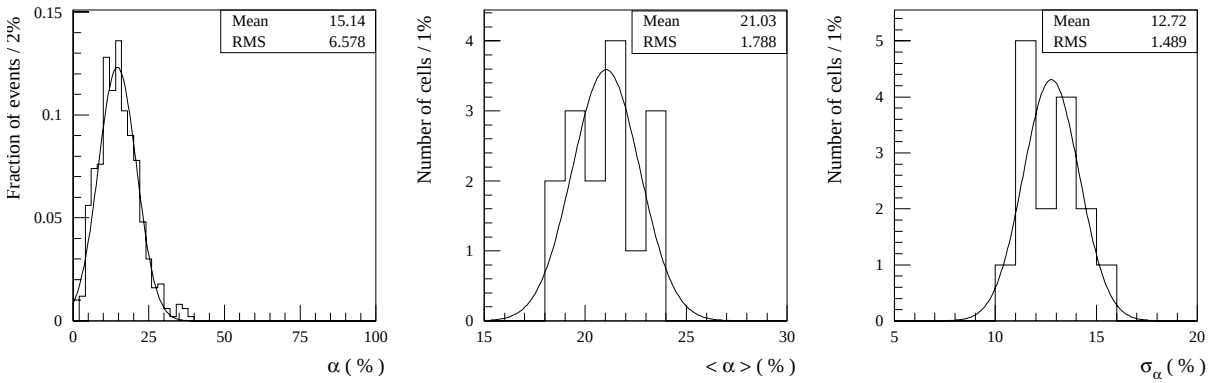

Figure 16: *Left:* typical distribution of α for MIPs. *Centre:* distribution of α mean value for MIPS over the 15 Ps cells studied. *Right:* distribution of α RMS for the same 15 Ps cells. Gaussian fits are superposed on the distributions.

The measured β and α mean values are a little pessimistic because of the time jitter of testbeam data with respect to the 40 MHz clock,which tends to lower β and to increase α. As already mentioned, this effect is however small: a decrease of β up to ~ 0.8 %.

The distributions of the RMS for β and α over the studied cells have mean values of 9.1 % for β and of 12.7 % for α. The contribution of the time jitter to these mean RMS values can be estimated using electron data with large photostatistics, where it dominates the RMS. In that case, the RMS was found to be of the order of 2 % for β and 3 % for α. By subtracting this time jitter contribution quadratically, the RMS measured for MIPs are decreased to 8.8 % for β and, respectively, 12.3 % for α.

5.1.3 Cosmic rays test bench measurements of the pulse shape

The cosmic ray test bench allows refined studies of the pulse shape thanks to a very short time sampling of only 0.4 ns. Figure 17 shows an example of the mean pulse shape obtained from one of the cells. No difference in the shape was observed for the mean pulses from different cells.

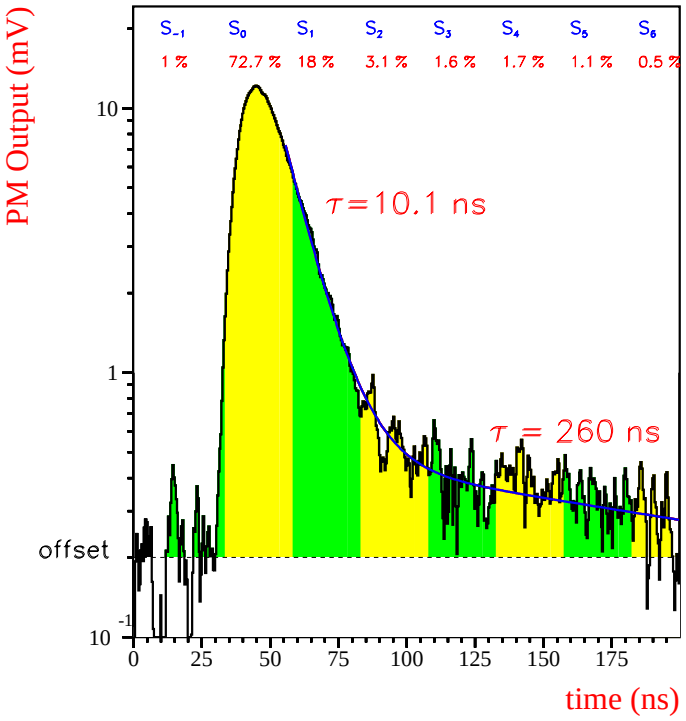

Figure 17: Mean pulse shape obtained for a cell of the cosmic bench. The 25 ns time windows are chosen in order to get the maximal fraction of signal in sampling 0. The fractions of signal integrated in the various time windows are reported. The data are well fitted by two exponentials with decay times of 10 and respectively 260 ns.

The pulse tail is well fitted by two exponentials: one with a fast decay time around 10 ns (9 to 11 ns are measured according to the channel) and a later one with a much longer decay time (greater than 200 ns). Only the first exponential is reproduced by the Monte Carlo simulations.

The offline computation of 25 ns time window giving the maximal fraction of signal in sampling 0 leads to results very similar to those obtained with the testbeam data. As for testbeam, the long term component has a non negligible effect beyond 50 ns (β_i, i $\geq$ 2). Maximal β_0 is found to be around 70 % on average, varying from 65 to 75 % according to the channel. It is few per cents lower than in testbeam data due to the higher RC of the readout: 5 ns (the capacity of the readout is dominated by the contribution of the monoanode photomultiplier, $\sim$ 50 pF, and the load resistor is 100 Ω), to be compared with the 1.5 ns of the testbeam readout.

5.2 Long term behavior

During the testbeam campaign, electron data were taken with 32 samples/event, in order to check the long term behaviour of the signals. The tail of the individual pulses are very erratic (see, by example, figure 18), but for a large number of them charges above the noise can be seen as long as 14 samples after the trigger signal.

By carefully selecting events without two signals in the data acquisition window and averaging all data available (about one hour of data taking), it can be seen that the tail

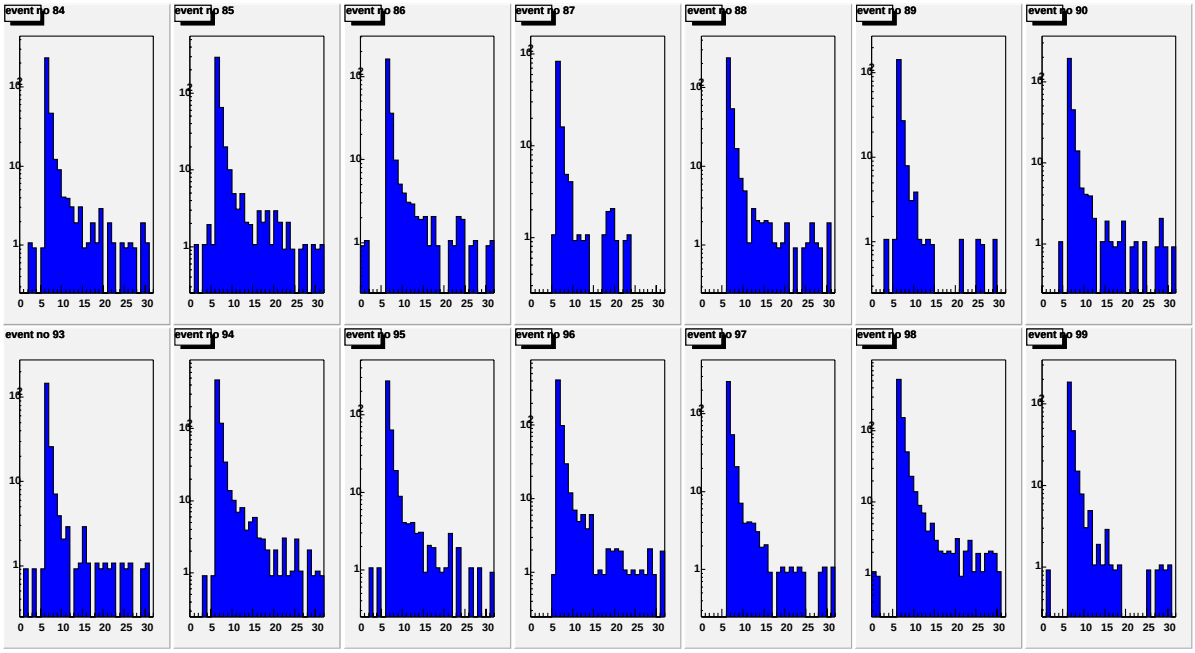

Figure 18: Some examples of individual pulses with 32 samples acquisition.

of the event is still noticeable 25 samples (i.e. more than 600 ns) after the trigger (fig 19). The selection of the events where the integrated charge on the other channels in samples other than the main one is less than 5 ADC counts does not change at all the signal shape. It can be therefore concluded that the effect is not due to crosstalk contributions from neighbouring channels.

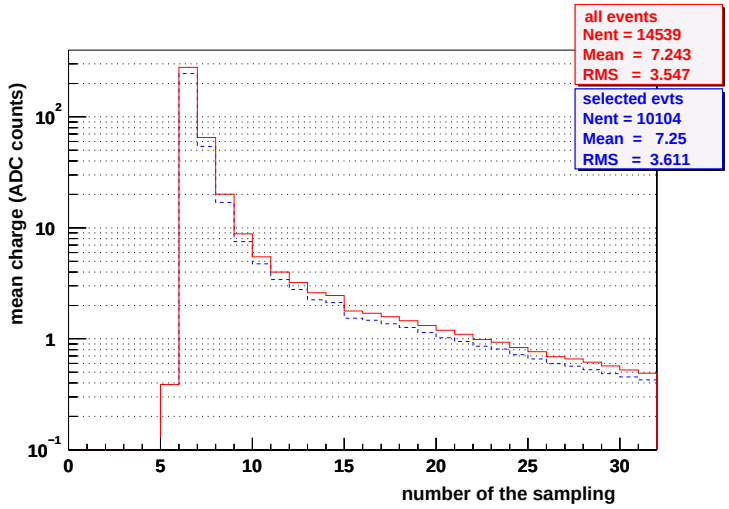

Figure 19: Signal shape, measured in the testbeam campaign with electrons: solid line for all events and dashes for events where less than 5 ADC counts are recorded on channels other than the one under study, in samples other than the main one.

We tried to reproduce these testbeam measurements in the lab. The injection of electrical signals directly in the PSVFEE board showed that the long signal tail is not an electronic problem (figure 20, right). Small PMT afterpulses are also unlikely to be (if at all) fully responsible for the effect: a similar MAPMT was directly illuminated in the lab with a LED and read out with the testbeam electronics (figure 20, left). A long term component is visible in the data, but is much lower than in the testbeam and no conclusion can be made on its origin, since the LED signal is not sufficiently sharp.

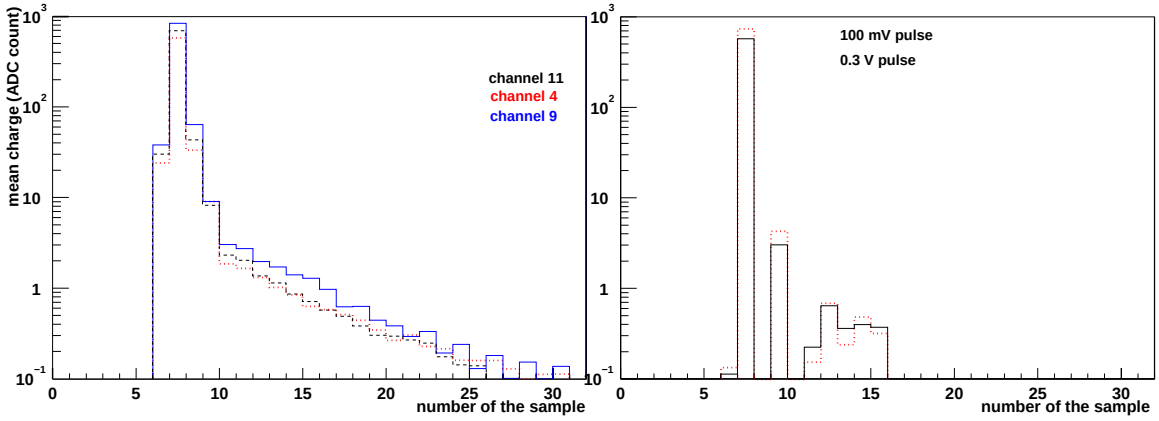

Figure 20: *Left:* averaged signal shape when LED light is injected directly into the PMT. The MAPMT HV is 700 V. Three different MAPMT channels were studied. *Right:* averaged signal shape when the MAPMT is shortcut and electrical pulses are injected directly into the PSVFEE board. The pulse generator is not good enough to eliminate the tail of the pulse.

Finally, we tested the dependence of these long term contributions on the total charge collected. For this, data were divided into nine different energy bins and the distribution of the total charge fraction collected in each sample as function of time was fitted with three exponentials. As example, for total charges between 400 and 500 ADC counts (figure 21) the distribution falls from about 70 % in sample 0 to less than 0.2 % in sample 26[1] and is well described by three exponentials with decay times of: 15 ± 0.04, 42.5 ± 0.7 and 288 ± 3 ns.

The three decay times rise with the charge collected (figure 22). The PMT saturation leads to a pulse enlargement and the rise of the first decay time with the charge appears therefore natural. The proportionality of the two others with the charge is unclear, as well as the nature of these long term contributions.

It is rather difficult to compare these results with the signal shape measurements in the cosmic rays test bench. The signal sampling of 25 ns is very poor compared to the first decay time, τ_1, and the result of the fit is necessarily larger than the real τ_1 value, since the raising time of the pulse is included in the main sample.

[1]The charge collected in sample 26 corresponds to the one deposited by 3 photoelectrons.

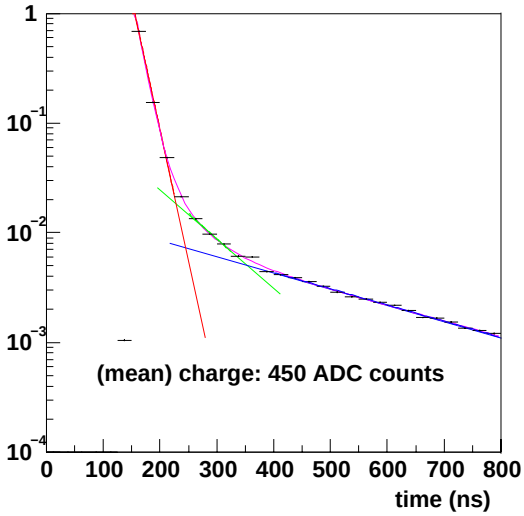

Figure 21: Distribution of the total charge fraction collected in each sample, as function of time (data points) and the three exponentials fit (magenta line). Exponential fits on restricted regions are also showed.

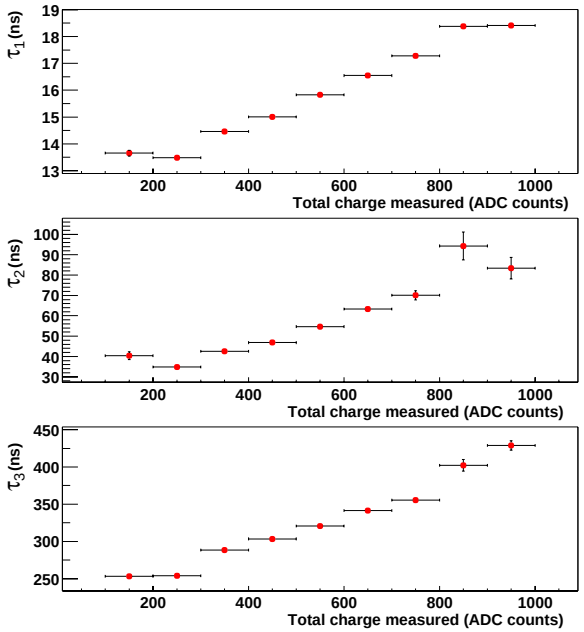

Figure 22: Variation of the three decay times with the total charge collected in the event.

As a conclusion, a long term component of the signal was observed in the testbeam data. It was checked that the effect is not related to the readout electronics, but it was not possible to conclude whether it comes from the MAPMT (afterpulses) or the upstream optics (fibres and scintillators). The effect was not reproduced on the testbench. Whatever the source of this long term component is, more than 88.4 % (95 %) of the pulse is recorded in the first 3 (8) samples.

5.3 Variation of the pulse shape with the pulse height

The variation of the pulse shape with the pulse height is characterised by the variation of α with the recorded number of ADC counts. Such a variation should be well accounted for in the LHCb experiment by implementing it in the PSFEE board to ensure a correct on average subtraction of the spill-over, over the full dynamic range.

This variation has been first studied keeping MIP signals and varying the MAPMT high voltage. Figure 23 makes use of 100 GeV muons recorded during June 2002 testbeam period and shows that in these conditions almost no variation is observed. It can be therefore concluded that the downstream electronics is almost free of non linearities that could affect α.

In a second time, the variation of α has been studied with electron data. The MAPMT high voltage is here fixed and variable pulse heights are obtained due to the large fluctuations in the energy that the electrons deposit in the Ps lead. Electron data are then binned with respect to the recorded number of ADC counts in the main sample, since this is the relevant quantity for LHCb.

Figure 24, left, was obtained with 50 GeV electron data recorded during August 2002 testbeam, at which the MIP point (see 5.1.2) was added. The different colors correspond

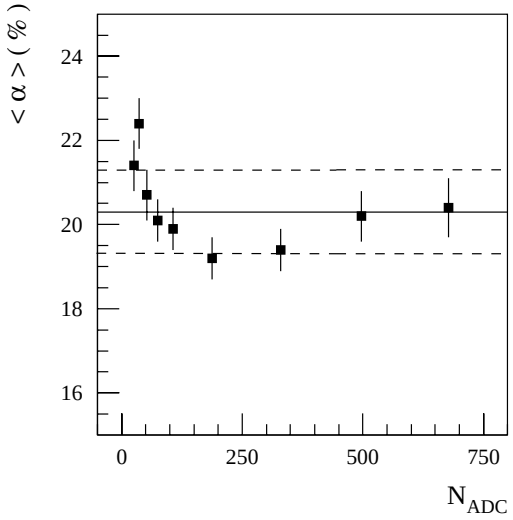

Figure 23: Mean values of α obtained for MIPs and MAPMT high voltages going from 700 V to 1000 V vs. mean numbers of ADC counts recorded in the main sample.

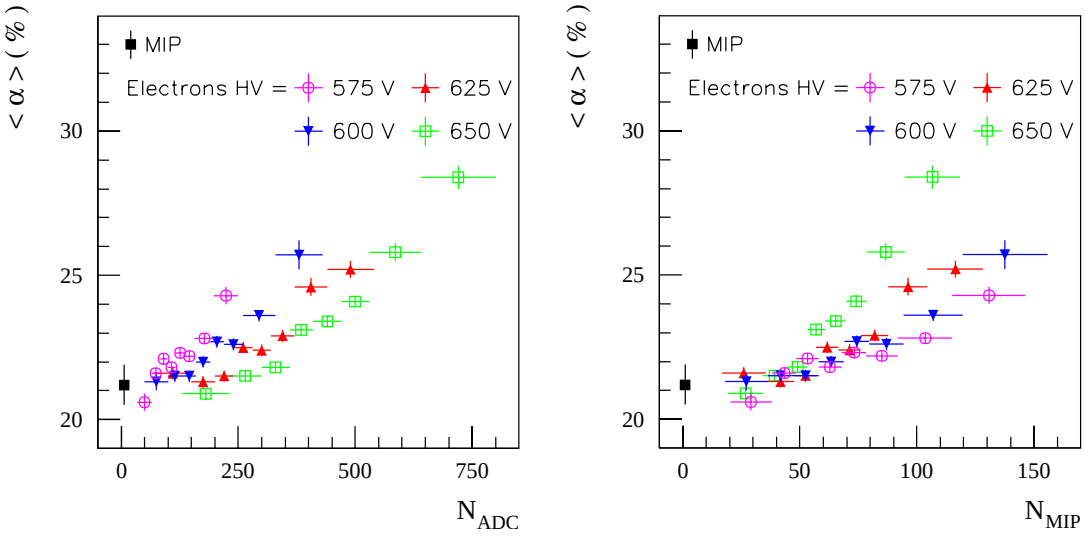

Figure 24: *Left:* mean values of α vs. recorded number of ADC counts in the main sample. Results obtained for electrons at four different MAPMT high voltages are reported. The MIP point has been extracted from MIP data. *Right:* same as before, but with the collected charge expressed in number of MIPs.

to the different high voltages at which the MAPMT was operated. The observed increase of α with the recorded number of ADC counts depends on the MAPMT high voltage and can therefore be attributed to an enlargement of the MAPMT pulse due to saturation effects.

To extrapolate these results to the LHCb case, the number of ADC counts should be scaled to the corresponding number of MIPs. MIP data, 100 GeV pions without lead sheet, were hence taken for each studied high voltage in order to get the conversion factors (see table 1). To calculate them, the mean MIP response was estimated from

High voltage (V)	Mean MIP response (ADC counts)
575	1.7
600	2.8
625	4.2
650	6.7

Table 1: Mean MIP responses for the four MAPMT high voltages used to characterise the variation of α seen in the electron data.

the mean value of a Gaussian fit performed over the MIP distribution, where the tail of the distribution, accounting for 20% of it, was discarded (see Section 7). This leads to figure 24, right, which shows that the effective variation of α decreases in fact by lowering the MAPMT high voltage.

The dynamic range of the Ps being limited to 100 MIPs, the relevant parameter is the difference between the α values at 100 MIPs and 1 MIP, $\Delta\alpha = \alpha_{100\mathrm{MIPs}} - \alpha_{\mathrm{MIP}}$. As the variation of α seems to be induced by MAPMT saturation effects, $\Delta\alpha$ has been reported as function of the MAPMT output current at 100 MIPs on figure 25. This output current has been evaluated by considering a gain of 4 of the PSVFEE chips and taking into account the fact that 150 Ω load resistors were used. On the same figure, a linear fit forced to pass through the origin is superposed to the data and shows that $\Delta\alpha$ is proportional to the MAPMT output current: at 1 mA, it gives a 5 % variation. Further physics studies are necessary in order to conclude how important is for the trigger and for the energy reconstruction to correct this variation of α with the energy. It should be noticed however that within the new design of the VFE electronics [9], the anode peak current is expected to be at maximum 200 μA (by considering a MAPMT gain non uniformity within a factor 2).

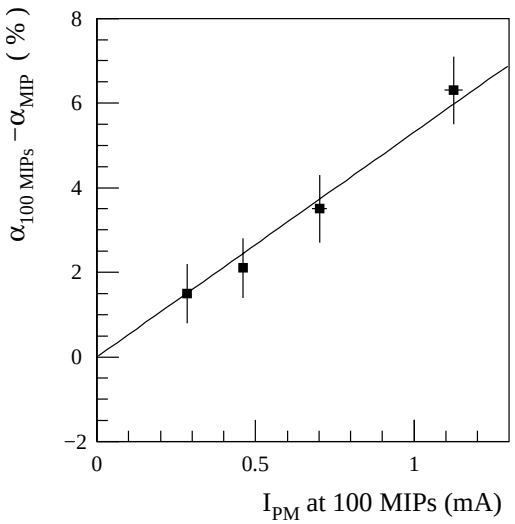

Figure 25: $\alpha_{100\mathrm{MIPs}} - \alpha_{\mathrm{MIP}}$ vs. MAPMT output current at 100 MIPs. The four points correspond to MAPMT high voltages of 575 V, 600 V, 625 V and 650 V.

6 Uniformity within a cell

The transversal uniformity was checked for one of the Ps cells, by scanning it with 50 GeV pions (quoted beam spread: $\sigma_{\rm hor} \sim 1$ cm, $\sigma_{\rm ver} \sim 1.6$ cm; ~ 1 % muon contamination with ~ 10 cm spread) in steps of 2 cm (49 measurements points). The total charge variation with the impact point on the cell is within few per cents and the same level of (non) uniformity is observed for β (figure 26).

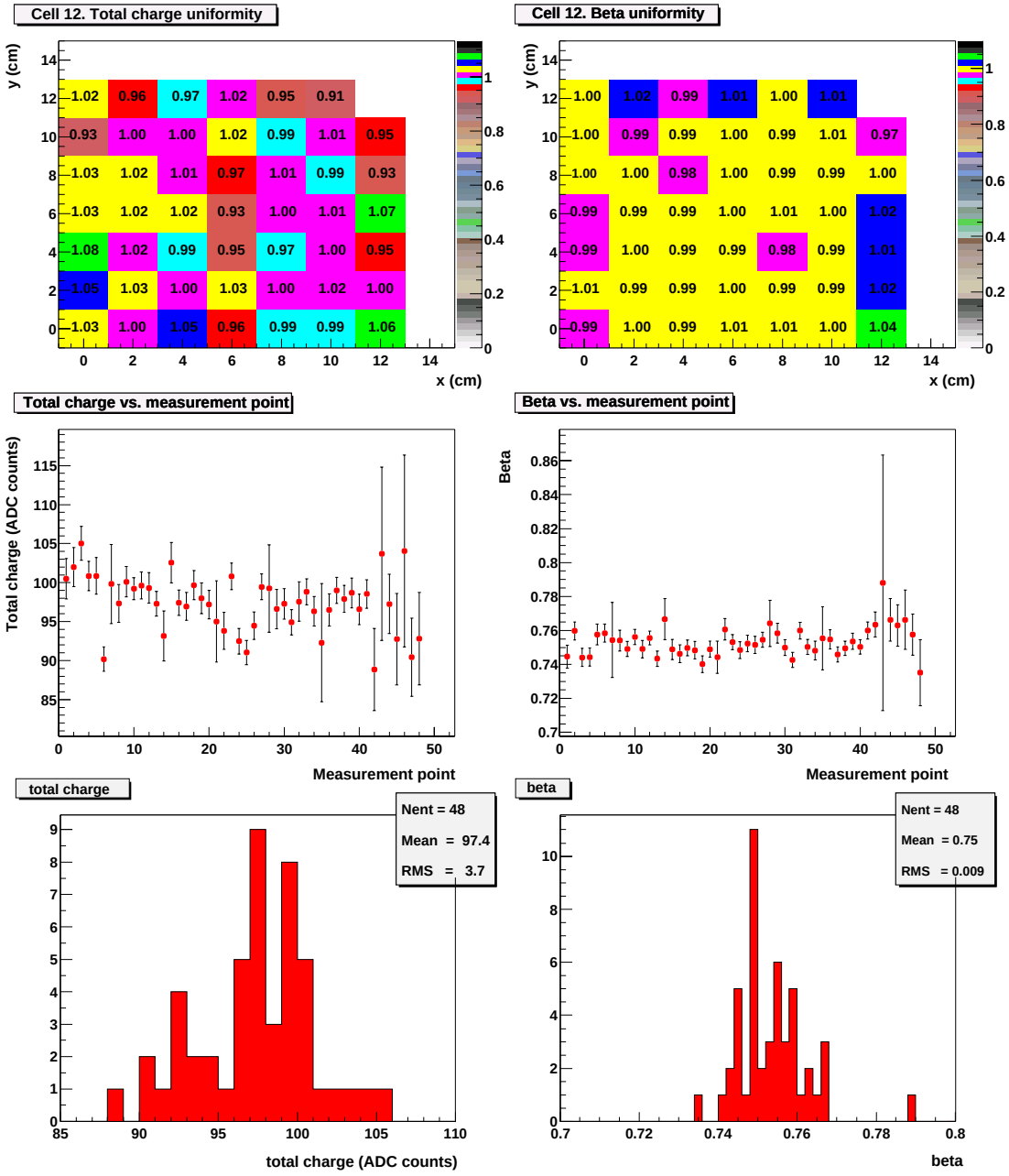

Figure 26: *Top:* map of the total charge collected (*left*) and of the β values (*right*) as function of the beam impact point on the Ps cell. The numbers give the ratios to the mean values over the whole cell. *Centre:* the total charge collected (*left*) and β values (*right*) vs. the measurement point. *Bottom:* charge (*left*) and β (*right*) distribution over the cell.

7 Light yield

An essential feature of the Ps module itself is the light yield of the different cells. Light yield should be large enough because the number of photoelectrons in the different pixels of the MAPMT dominates the resolution on the energy deposited in the Ps. Light yield should also be uniform over the cells of the module since it is intended that the tuning of the load resistors will only correct the MAPMT non uniformities.

The relevant parameter to characterise the light yield is the number of photoelectrons per MIP. It can be estimated from MIP data with the formula:

$$N_{pe/MIP} = (\mu_{MIP}/\sigma_{MIP})^2,$$

where μ_{MIP} is the central value of the collected charge distribution and σ_{MIP} its spread.

This calculation is approximate since the distribution of the MAPMT signals depends upon the Landau distributed energy loss in the scintillator. Furthermore, due to the finite MAPMT gain, statistical fluctuations at the very first dynodes induce an underestimation of the number of photoelectrons. The first effect has been investigated by scaling the MIP signal to a large LED pulse:

$$N_{pe/MIP} = N_{pe/LED} \times (\mu_{MIP}/\mu_{LED}) = (\mu_{LED}/\sigma_{LED})^2 \times (\mu_{MIP}/\mu_{LED}),$$

where appear both the central value and the spread of the LED distribution, μ_{LED} and σ_{LED} respectively, but only the central value of the MIP distribution. The last effect requires analytical corrections that will be discussed in a dedicated paragraph. However, only the effective number of photoelectrons is considered at first : it characterises the spread of the charge distribution and is obtained without applying these corrections.

The effective number of photoelectrons per MIP for the different cells was measured using the two approaches described above. For this, MIP (100 GeV muons in June 2002 and 100 GeV pions without lead in August 2002) and LED data were recorded with the same 800 V MAPMT high voltage. The charge was integrated over 125 ns in June 2002 and over 200 ns in August 2002. These time windows are large enough to collect more than 98 % of the total charge. Figure 27 shows two examples of charge distribution obtained for MIP and LED signals. The Gaussian fits used to estimate the central value and the spread of these distributions are superposed to the data. While the LED distribution is Gaussian, the Landau tail clearly appears on the MIP one. For MIPs, the Gaussian fit was therefore limited to the lower part of the distribution, which contains 80 % of the events. The estimation of the effective number of photoelectrons per MIP from MIP data depends therefore slightly on the definition of the "Gaussian" part of the distribution. The method which scales the MIP signal to a large LED pulse is much more stable since it does not use the estimation of the spread of the MIP distribution.

Figure 28, left, shows the effective number of photoelectrons per MIP measured for the different cells. This number was estimated for both June and August 2002 by using only MIP signals and the results are compatible for the two testbeam periods. They are also consistent with the ones obtained by scaling MIP signals to LED pulses using the August 2002 data. Figure 28, right, shows the distribution of the effective number of photoelectrons per MIP over the 16 cells of the Ps module. It was obtained by combining the results from the two alternative approaches. A Gaussian fit performed with the maximum log-likelihood method is superposed to the data. From cell to cell, the effective number of photoelectrons per MIP varies from 9.9 to 18.2 with a mean value of 14.8 and a RMS of 2.3.

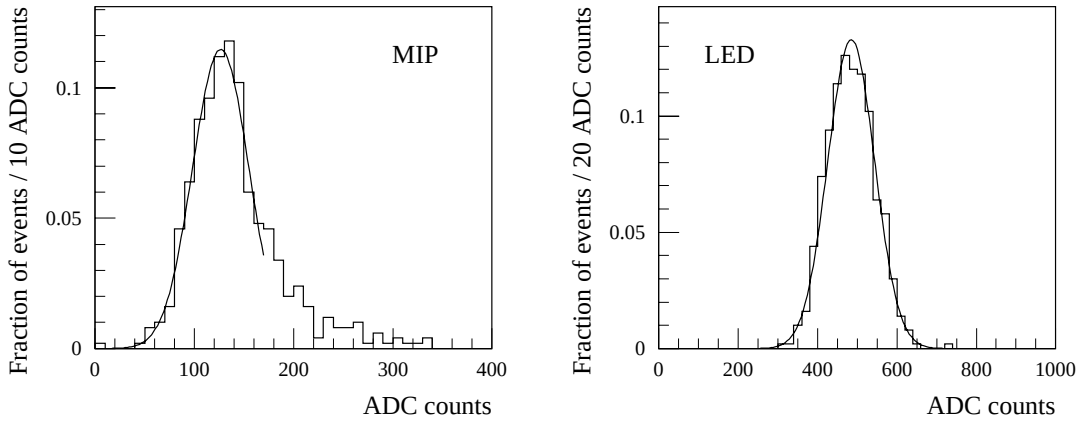

Figure 27: Typical distributions of charge deposited by MIPs (left) and LED photons (right).

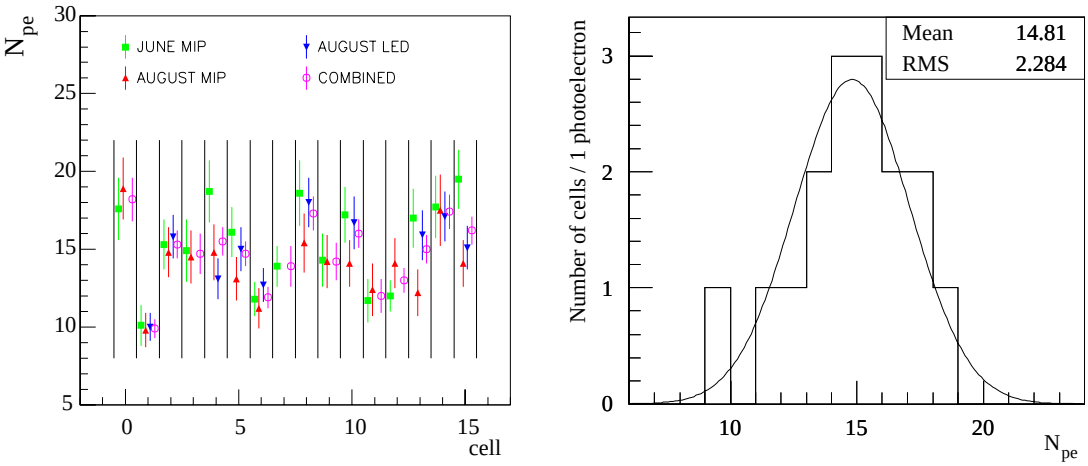

Figure 28: *Left:* effective number of photoelectrons per MIP for the 16 cells under study, as obtained from the different estimations (using only MIP signals: JUNE MIP and AUGUST MIP; or scaling MIP signals to LED pulses: AUGUST LED) and from their combination (COMBINED). *Right:* distribution of the effective number of photoelectrons per MIP over the 16 cells of the Ps module.

The mean value is lower than the 20 pe/MIP quoted in the LHCb calorimeter TDR [1] for 12×12 cm^2 cells. This is due to the 80 cm of WLS fibres used in the testbeam to extract the light from the Ps module: considering an attenuation length of 286 cm for the Kuraray Y11 WLS fibres [10] effectively leads to 25 % light loss.

As already mentioned, the effective number of photoelectrons discussed above is an underestimation of the true number of photoelectrons collected on the first dynode. Taking into account the enlargement of the charge distribution due to statistical fluctuations on each dynode, the true number of photoelectrons per MIP is found to be ~ 18.0. This is the relevant parameter for the simulation of the event by event fluctuations of the light shape. On the other hand, the high voltage used here is 800 V and corresponds to MAPMT gains of the order of 10^6. The effective number of photoelectrons per MIP

is therefore overestimated with respect to the one corresponding to the nominal gain of 5×10^4 which is found to be ~ 13.6. Moreover considering the fact that only 73 % of the charge is integrated within 25 ns, it decreases to ~ 9.9. This last number therefore characterises the spread of the charge distribution when taking into account the nominal MAPMT gain and the 40 MHz readout.

The cell to cell relative dispersion is rather large. The following ratios are observed: RMS/average = 15 % and maximum/minimum = 1.8. Part of these fluctuations are coming from MAPMT photocathode non uniformities and so would not contribute to non uniformities of the Ps response in LHCb. Nevertheless, the typical quantum efficiency non uniformity of the MAPMT is within a ratio maximum/minimum of the order of 1.2 [11]. This means that the light yield ratio between the brightest optical channel and the least bright one is at least of the order of 1.5. This would lead to a too high non uniformity of the Ps response and should be reduced for production modules by improving the optics such as the connection between the clear fibres and the MAPMT.

Figure 29 shows the mask used for this connection during 2002 testbeam periods. It is far away from the final design in which all the fibre pairs will be parallel in order to have the same coupling for all the MAPMT pixels. This is a very important feature because the very large non uniformities which were observed inside the MAPMT pixels are mainly due to the layout of the entrance optics and are therefore rather well reproduced from one pixel to another. The final mask will include in addition a precise self positioning system. During 2002 testbeam periods, the mask was positioned by minimising the crosstalk on neighbouring pixels. This was only done on one pixel and with a relatively poor precision of ~ 0.2 mm. The crosstalk between pixels depends also heavily both on the orientation of the fibre pairs and on the mask positioning (see section 10).

Figure 29: Close-up of the fibres to MAPMT mask used during 2002 testbeam periods.

8 MAPMT gain

The knowledge of the variation of the MAPMT gain over the 16 used pixels is mandatory to measure properly the crosstalk between channels. It can be derived from the number of photoelectrons estimated in the previous section. The relative gain of each electronic channel is first defined as the ratio between the mean number of recorded ADC counts and the corresponding number of photoelectrons. The relative gains are then normalised to their average value. Figure 30, left, shows that compatible results are obtained for the three analysis. It also shows the distribution of the relative gain of the electronics over the 16 cells of the Ps module, obtained by combining the results of the different analysis. A Gaussian fit performed with the maximum log-likelihood method is superposed to the data. The distribution has a RMS of 0.18 and a maximal dispersion maximum/minimum = 1.30/0.69 = 1.88, which is in good agreement with the typical gain dispersion of the used MAPMT [12].

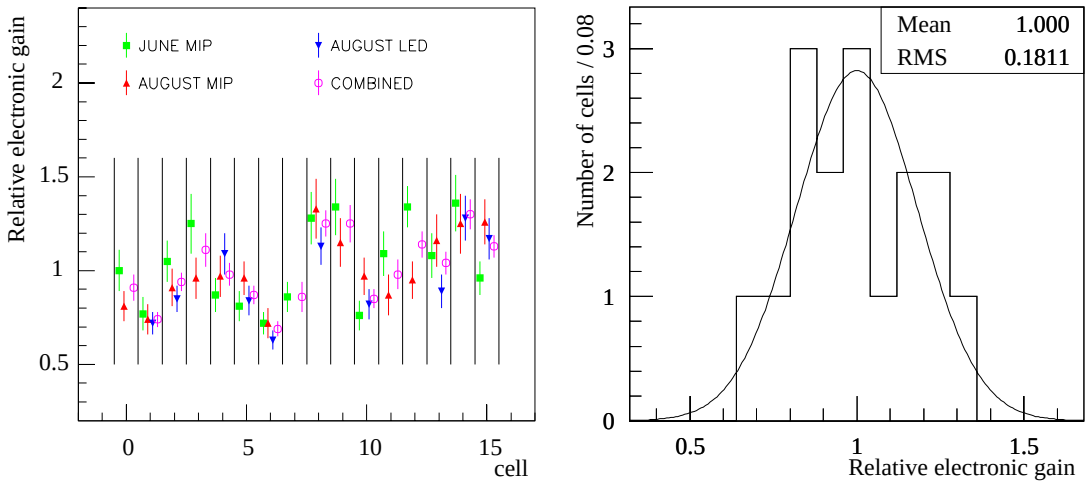

Figure 30: *Left:* relative gain of the electronic channels used to read out the 16 Ps cells, as obtained from the different estimations of the number of photoelectrons per MIP. *Right:* distribution of the relative gain of the electronic channels used to read out the 16 cells of the Ps module.

During June 2002 testbeam period, the MAPMT gain dependence on the high voltage was checked by recording 100 GeV muons on the same cell and by varying the MAPMT high voltage from 500 V to 1000 V. Figure 31 shows the number of ADC counts, obtained by integrating the MIP signals over 125 ns, as a function of the applied high voltage. The reported values of the charge were obtained as mean values from Gaussian fits performed over the "Gaussian" part of the MIP distributions (see figure 27). Data are well fitted with a gain parametrisation as $G = \alpha V^{\beta}$. The result of the fit is superposed to the data. It gives a β of 10 which is a typical value for the used 12 stages MAPMT.

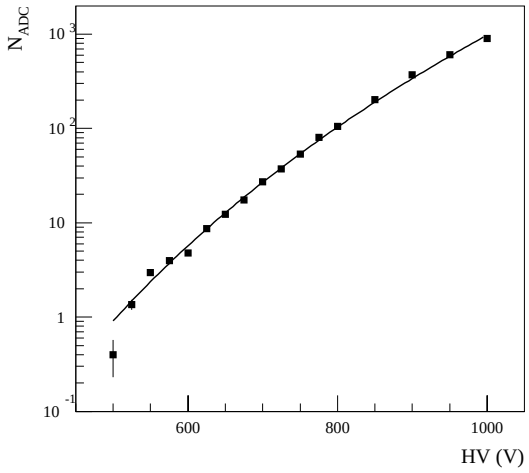

Figure 31: Gain dependence on the MAPMT high voltage.

To investigate the possible effect of the variation of the MAPMT high voltage on the uniformity of the Ps response, MIP data were recorded on four different cells with high voltages going from 575 V to 750 V during August 2002 testbeam period. The same Gaussian fit as before is used to estimate the central MIP response and, as uniformity of the Ps response is concerned, only signals integrated in the main 25 ns sample were considered. Figure 32 shows the obtained results. Left plot shows that the four cells clearly exhibit the same behavior. Going further, the gains of the four cells are first normalised to their 650 V values : G(HV)/G(650 V). Taking one cell as reference, normalised gain ratios [G(HV)/G(650 V)] / $[\mathrm{G(HV)/G(650\ V)}]_{\mathrm{ref}}$ are then computed for the three other cells. The right plot of figure 32 shows their evolution with the high voltage. They are found to be statistically compatible with the unity. Between 575 V and 750 V, the gain is increased by more than a factor 28. Even in this very wide range of gains, high voltage changes have a very limited impact on uniformity. The induced non uniformity is lower than 5 %.

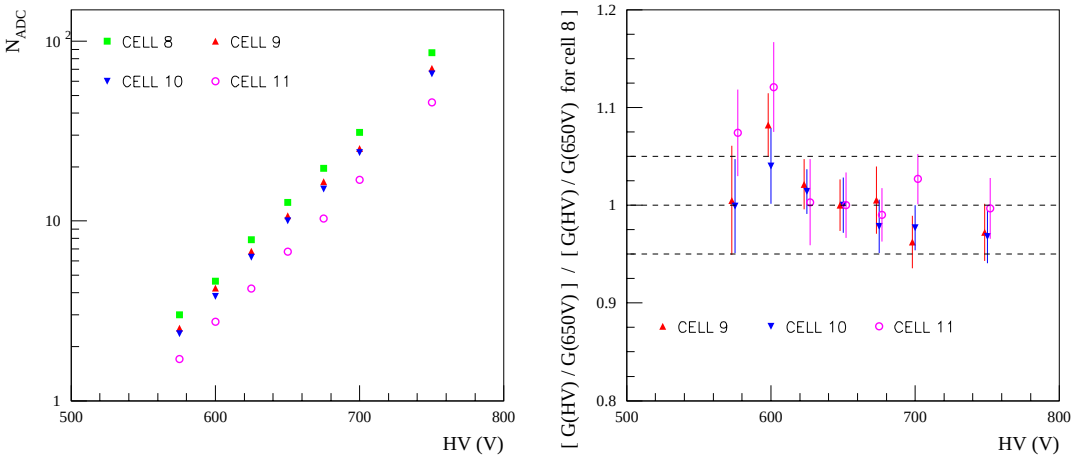

Figure 32: Test on 4 cells of the effect of MAPMT high voltage changes on the uniformity of the Ps response. *Left:* number of ADC counts vs. high voltage for the 4 cells. *Right:* [G(HV)/G(650 V)] / $[\mathrm{G(HV)/G(650\ V)}]_{\mathrm{ref}}$ vs. high voltage for 3 of the 4 cells, the other one being used as reference.

9 Integrator gain

Gain fluctuations within the half-channels of the integrators have been investigated using MIP and LED data recorded during August 2002 testbeam period (the same data as quoted in section 7). Since half-channel gains are concerned, only signals integrated in the main 25 ns sample are considered here. Data are divided into two samples corresponding to each of the two half-channels, called "Odd" or "Even". For each half-channel, the average response to MIP and to LED photons is estimated from the mean value of a Gaussian fit over all the distribution. There is no special treatment of the MIP Landau tail because the statistics is limited.

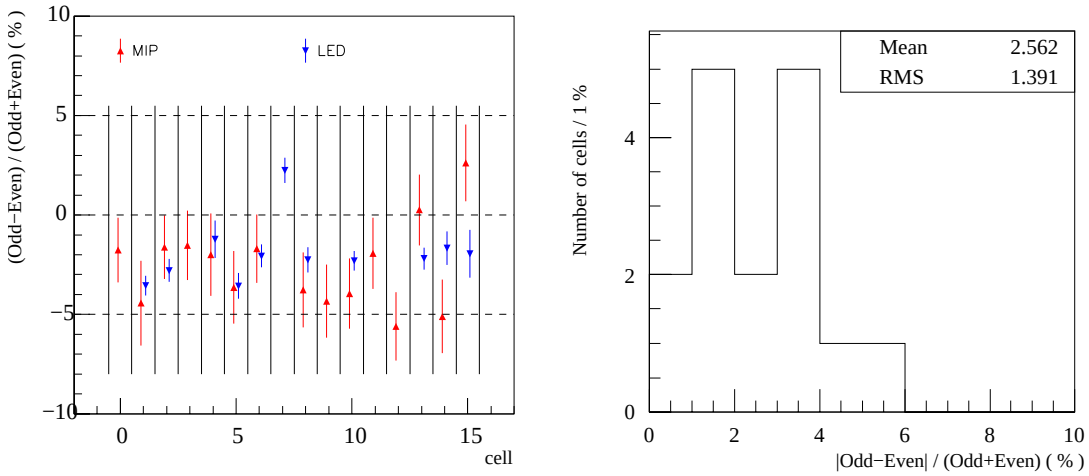

Figure 33: *Left:* half-channel gain relative differences for the 16 cells under study, as they were obtained from MIP and LED data. *Right:* distribution of the half-channel gain relative difference over the 16 cells of the Ps module.

For each cell, the relative difference between the gain of the two half-channels is defined as the ratio $(\text{Odd} - \text{Even})/(\text{Odd} + \text{Even})$. Figure 33 shows that compatible results have been obtained using MIP and LED data. The LED determination is rather precise, the typical error being around 0.5 %. It also shows the distribution of the relative difference between the gains of the 32 half-channels used, obtained by combining both analyses. The maximal difference is around 5 % and the average one 2.6 %. These results are in good agreement with laboratory measurements of the integrators (see figure 34).

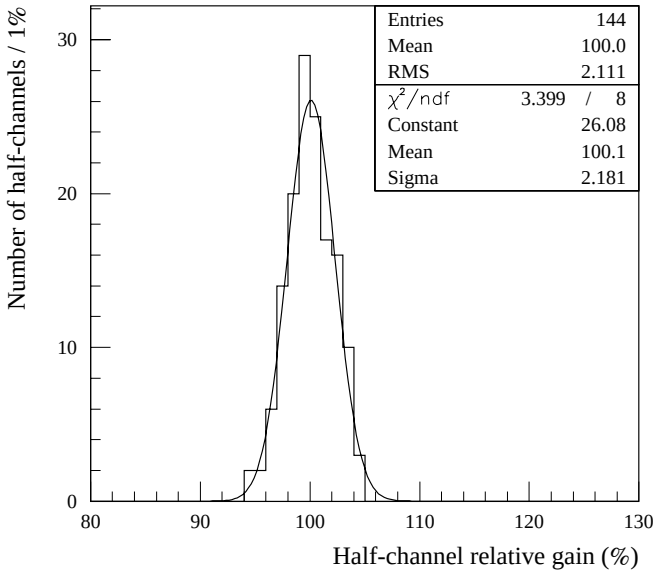

Figure 34: Distribution of the half-channel gain (%), as obtained from laboratory measurements of the standalone chips. 9 chips were tested, leading to a total of 144 half-channels. The gains are normalised to their average value.

10 Crosstalk

During June and August 2002 testbeam periods, crosstalk was investigated by firing one of the Ps cells with 100 GeV electrons. Crosstalk on each other cell i is estimated by computing the ratio between its output and the output of the fired cell, (cell i)/(fired cell). The cell outputs correspond to signal integrations over large time windows of 175 ns and 200 ns respectively, for June and August 2002 data. Crosstalk is first defined as the mean value of a Gaussian function fitting the peak of (cell i)/(fired cell) distribution (see figure 35). The differences of gain between channels are then corrected using the combined determination of relative electronic gains reported in section 8. Figure 36 shows the obtained crosstalk. The relative precision of these measurements is of the order of 10 %. Some crosstalk is observed between both MAPMT pixels and Ps cells.

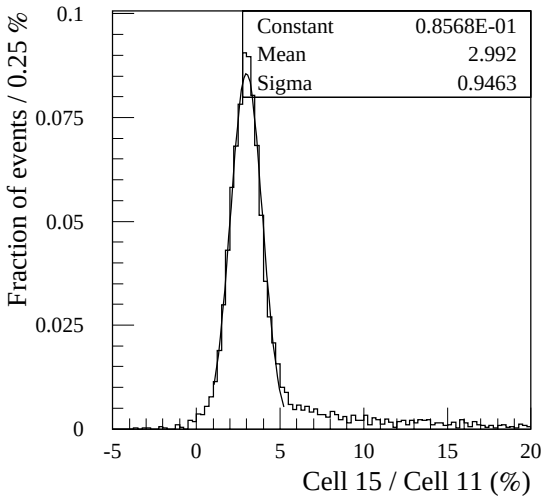

Figure 35: Example of an event by event crosstalk distribution.

Summing the eight neighbouring pixels, the global crosstalk at the level of the MAPMT was found to be around 18 %. In June, up to 6.4 % crosstalk was measured on the most exposed pixel, whereas in August this maximum decreased to 4.3 %. The large difference between the pixel repartition of the crosstalk observed in June and August measurements shows the importance of setting accurately the fibres in the MAPMT mask and the mask itself. As already mentioned in section 7, the used mask (see figure 29) is very different from the final one. Neither the orientation of the fibre pairs, nor the mask position were well controlled. The situation must necessarily be better with the final mask.

Furthermore, testbeam data clearly show unexpected crosstalk between the cells of the Ps. It is measured to be around 2 to 3 %. This was confirmed with the cosmic rays bench using LEDs installed on the surface of the Ps cells. LEDs were very well isolated to avoid any light leakage. Thanks to the specially designed PMT mask (see figure 5), there is no crosstalk at the level of the mono-anode PMT and standalone cell to cell crosstalk can be characterised. Figure 37 shows an example of the crosstalk measurements done with the cosmic bench. Crosstalk is clearly observed on the four cells bordering the one fired with the LED. To investigate this crosstalk between Ps cells, the transparency of

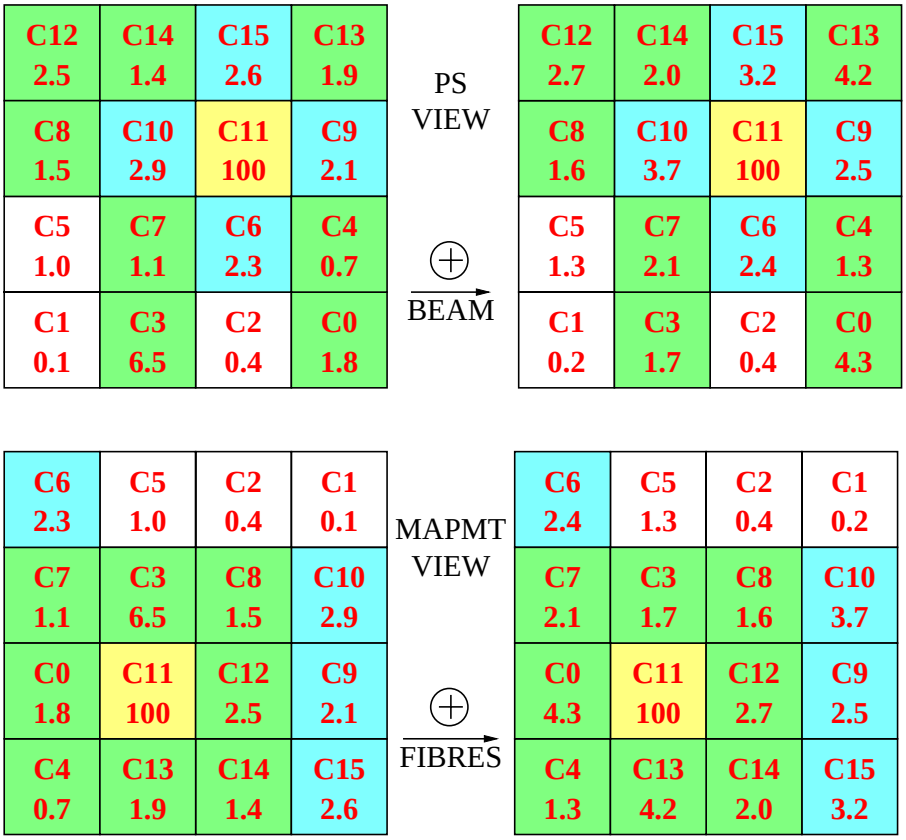

Figure 36: Crosstalk measured in testbeam (%). Left column corresponds to June 2002 results, right one to August 2002 results. Crosstalk measurements are presented with respect to a view of the Ps module (first raw) and to a view of the MAPMT (second raw).

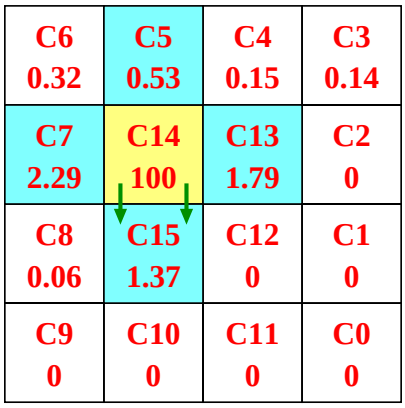

Figure 37: Standalone cell to cell crosstalk measured with the cosmic bench (%).

the paper used to wrap the cells (Tyvek 1059D) was measured with a mono-anode R-5900 PMT illuminated by a LED through an optical fibre and a light mixer, by introducing paper sheets in between the light mixer and the PMT. The fraction of light transmitted through two sheets of the used paper was estimated to 5 %. Almost the same result was found for the paper that will be used for production modules (Tyvek 1060B). Insufficient

cell wrapping was therefore identified as the origin of this cell to cell crosstalk. For the production modules, it has been requested to place an additionnal absorber between the Ps cells.

The standalone electronic crosstalk was also measured by reproducing all the electronic chain from the output of the MAPMT to the input of the PSFEE board. Figure 38 shows the results that were obtained. Low crosstalk of 0.3 % is observed between few neighbouring cells at the level of MAPMT output. Up to 1 % crosstalk is measured between neighbouring cells at the level of PSVFEE board output. This crosstalk was indentified as coming from the PSVFEE board itself. In particular, individual characterizations of the integrator chip have led to very little crosstalk of few per thousands. The used PSVFEE prototype measures 15×15 cm^2 while the final board will measure around 8×8 cm^2. The induced wire length reduction will necessarily reduce this crosstalk.

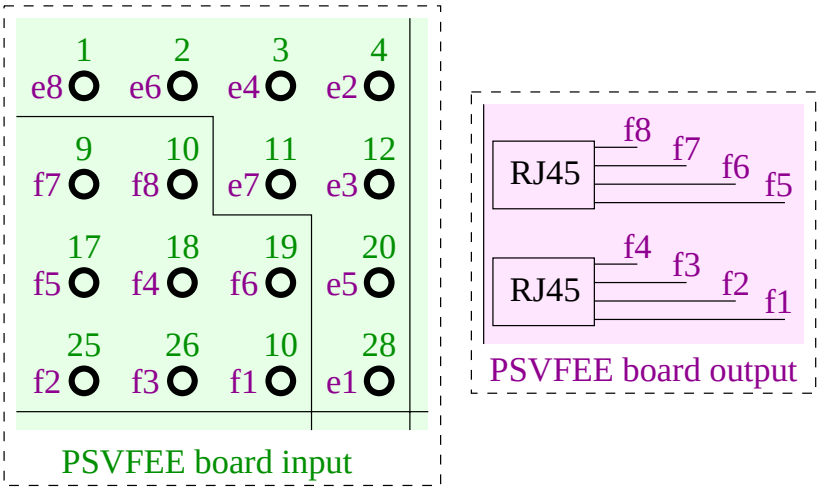

	10	9	19	17	18	26	25	27
f8	100	0	0	0	0	0	0	0
f7	0.3	100	1.0	0	0	0	0	0
f6	0	0.7	100	0.7	0.3	0	0	0
f5	0	0	0.7	100	0.3	0	0	0
f4	0	0	0.3	0	100	1.0	0	0
f3	0	0	0	0	1.0	100	1.0	0
f2	0	0	0	0	0	1.0	100	0
f1	0	0	0	0	0	0	0	100

Figure 38: Measurement of the standalone electronic crosstalk. *Top:* disposition of the electronic channels at the input (left) and the output (right) of the PSVFEE board. *Bottom:* relative responses (%) of the different output channels for each input channel, normalised to the response of the output corresponding to the input.

11 Conclusions

The experimental status of the preshower system was summarised. Two prototype modules and a complete prototype of the readout chain (MAPMT, VFE and FE electronics) have been tested in a testbench developed at LPC and in testbeam campaigns in June and August 2002.

The readout electronics is stable, with a noise level less than 1 ADC count. The measurements of the MAPMT and integrator gains are consistent with the standalone measurements in the laboratory.

On average, 73% of the MIP signal is integrated in 25 ns and the spillover from a BC to the next one is 21% of the first BC signal.

The preshower cells are found to have an uniform response over their surface. The light yield is consistent with the 20 pe/MIP quoted in the LHCb calorimeter TDR, when the WLS fibres length is scaled up to the actual length. The dispersion of the light yield from different cells is too large and it will be necessary to reduce it for production modules. However, an important contribution to this dispersion comes from the MAPMT mask used, which is not satisfactory.

A large crosstalk was measured and its source was traced down to the present MAPMT mask and to insufficient cell wrapping. Both the mask and the wrapping should be improved for production.

References

[1] *LHCb Calorimeter Technical Design Report*, CERN/LHCC/2000-0036 (2000).

[2] Bohner, G *et al.*, "Very front-end electronics for the LHCb preshower", LHCb Note LHCb-2000-047 (2000).

[3] *LHCb Technical Proposal*, CERN/LHCC 98-4, LHCC/P4 (1998).

[4] Bohner, G *et al.*, "Front-end electronics for LHCb preshower", LHCb Note LHCb-2000-048 (2000).

[5] E. Aguilo, "Recent Ps/Spd pulse shape simulation results", LHCb Calorimeter Software Meeting, 19 February 2002.

[6] F. Camarena *et al.*, "Characterisation of the new 8 stages Hamamatsu photomultiplier for the July 1998 Test Beam", ATLAS Note, ATL-TILECAL-98-166 (1998).

[7] M. Fiandino, "Conception et réalisation d'un driver pour la carte PSFEE du détecteur LHCb", rapport de stage de 3$^{\text{ème}}$ année ISIMA (2002).

[8] See http://root.cern.ch/

[9] Jacques Lecoq, "Status of PS chip", LHCb Calorimeter Meeting, 10 December 2002.

[10] *ATLAS Tile Calorimeter Technical Design Report*, CERN/LHCC/96-42 (1996).

[11] Hamamatsu private communication.

[12] E. Aguilo *et al.*, "Mean Current in Ps/Spd MultiAnode PhotoMultipliers Tubes", LHCb Internal Note LHCb-2003-003 (2003).